International Journal of Heat and Mass Transfer

Large Eddy Simulations of High-Heat-Flux Supercritical CO_2 Convection in Microchannels: Mixed Convection and Non-uniform Heating

Mahdi Nabil
Department of Mechanical and Nuclear Engineering
The Pennsylvania State University
University Park, PA, 16802
Mahdi.Nabil@psu.edu

Alexander S. Rattner[1]
Department of Mechanical and Nuclear Engineering
The Pennsylvania State University
University Park, PA, 16802
Alex.Rattner@psu.edu

Abstract

Near-critical-point supercritical fluid convection is a promising solution for emerging high-flux thermal management needs because of the high fluid thermal conductivities and specific heats. Supercritical convection has been extensively studied for large diameter channels with uniform heating ($4.1 < D < 22.7$ mm, $0.05 < q'' <$ 330 W cm^{-2}). However, limited information is available on transport processes to guide engineering of high-flux compact supercritical heat transfer equipment, which often have non-uniform heating distributions. To address this need, large eddy simulations (LES) are employed to study supercritical CO_2 convection in microchannels (750 µm × 737 µm cross-section). First, the simulation approach is validated with published experimental data. Studies are then conducted for horizontal isothermal heated channels at reduced pressure $P_r = 1.1$, mass fluxes $G = 100 - 1{,}000$ kg m^{-2} s^{-1} (Re $= 3{,}000 - 35{,}700$), average wall heat fluxes $q'' = 24 - 62$ W cm^{-2}, and bulk flow temperatures $T_{bulk} = 291 - 317$ K (inside and outside pseudocritical range). Results are used to assess the applicability of published supercritical convection correlations for microchannel heat exchangers. All available supercritical correlations are found to under-predict heat transfer coefficients at high heat fluxes ($q'' = 58 -$ 62 W cm^{-2}). The bottom-to-top wall heat transfer coefficient (HTC) ratios from these cases are used to determine a new criterion for the onset of significant mixed convection effects. At low mass fluxes ($G =$ 100 kg m^{-2} s^{-1}), this HTC ratio is found to exceed 2.5×. Simulations indicate that, at these conditions, increased heat fluxes lead to reduced HTCs for low and high mass fluxes, but increased HTCs at intermediate mass flux values. Finally, an illustrative case is evaluated to assess the impact of conjugate heat transfer effects in microscale supercritical convection, and highlight limitations of conventional modeling approaches. This study quantifies the accuracy of convection correlations for high-heat-flux microchannel pseudocritical conditions, provides new criteria for

[1] Corresponding author:
Address: 236A Reber Building, University Park, PA 16802
Email: Alex.Rattner@psu.edu

predicting the onset of mixed convection in microchannel supercritical flows, and demonstrates the impact of conjugate heat transfer effects in microchannel supercritical heat exchangers.

Keywords

Supercritical fluid; Carbon dioxide; Microchannels; Heat exchanger; Large eddy simulation; Mixed convection

1. Introduction

High-heat-flux thermal management technologies are critical enabling components of many engineering systems, including microelectronics [1,2] and solar-thermal power production [3]. Supercritical carbon dioxide (sCO_2) has extremely high volumetric heat capacity and thermal conductivity in the pseudo-critical range (7.5 – 8.5 MPa, 30 – 40°C), potentially enabling high heat flux thermal management (~500 W cm^{-2}), improved device-surface temperature uniformity, and reduced pumping loads compared with liquid and two-phase cooling solutions [4]. A representative plot is presented in Fig. 1 comparing the c_p of sCO_2 at constant reduced pressure $P_r = 1.1$ with those of subcritical liquids commonly employed in thermal management applications. Unlike the familiar boiling phase-change process, supercritical fluids undergo a continuous, non-isothermal transition from "liquid-like" to "gas-like" properties during heating without formation of a sharp interface. Additionally, supercritical heat transfer may avoid the potential for boiling instabilities and dryout. CO_2 has a low GWP (= 1) and is non-toxic, non-flammable, and low cost.

Supercritical Brayton cycles have emerged as a national strategic focus for highly efficient solar thermal, geothermal, nuclear, and clean fossil energy systems [5]. Key advantages of these cycles include improved thermal efficiency, smaller components, and a reduction of fresh water consumption in electricity production, which presently accounts for 45% of U.S. fresh water withdrawals [6]. Supercritical Brayton systems are capable of using high temperature solar-thermal heat more efficiently than conventional steam cycle power plants, and are more compact than equivalent steam power plants [7]. Current generation concentrated solar power tower designs operate at peak receiver heat fluxes of ≳150 W cm^{-2} and temperatures of ~650°C [8], which limit capture (~80%) and cycle (~40%) efficiencies. Recent studies have demonstrated that sCO_2 based-technologies have the potential to increase concentrating solar plant efficiency from 42% (with boiling water) to nearly 50% [9], significantly reducing plant size and electricity cost. Advanced high-flux thermal management will enable reduced collector sizes and increased fluid temperatures, improving overall plant performances.

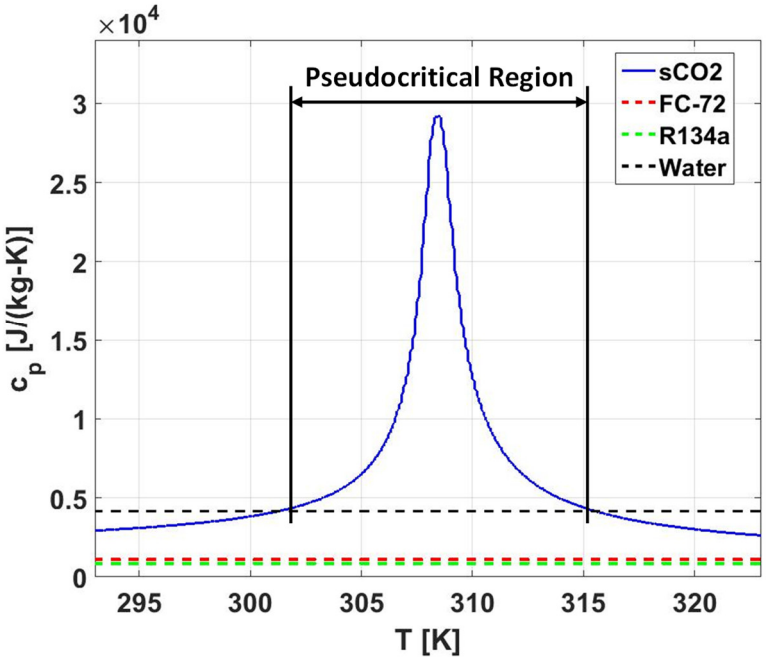

Figure 1. Specific heat capacity c_p of sCO_2 at $P = 8.1$ MPa, compared with conventional subcritical liquid coolants

Two distinct phenomena have been identified that affect supercritical heat exchanger performance. *Heat transfer deterioration* can occur due to concentration of high temperature vapor-like film near walls. This effect can occur for all wall orientations. In a second phenomenon, low-density plumes rise from upward facing heated surfaces, locally enhancing heat transfer coefficients (HTCs) due to *mixed convection* [10,11]. This process displays similarities to subcritical film boiling. Although these two phenomena have been reported in the literature, consensus on the underlying mechanisms driving heat transfer deterioration/enhancement and flow instabilities remains elusive [12].

Supercritical CO_2 heat transfer has been employed in industrial processes since the 1960s [13]. However, transport behavior has generally been characterized empirically and for limited operating ranges. In an early experimental study in the 1950s, Bringer and Smith [14] studied sCO_2 heat transfer in a constant heat flux horizontal pipe, and proposed a simplified empirical heat transfer model of the form $\mathrm{Nu} = a\mathrm{Re}^b\mathrm{Pr}^c$, similar to the Dittus-Boelter [15] equation. In their model, property values were evaluated at a specified reference temperature. Bringer and Smith [14] found that this approach had limited accuracy near the critical point where sharp property variations are encountered. Other prior experiments with sCO_2 [16–19] have focused on large diameter ($4.1 < D < 22.7$ mm), uniformly heated circular tubes. Lumped wall-to-bulk property difference correction factors have been proposed for predicting convection in plain large-diameter channel flows [16,20–23].

Prior to the present computational investigation, which is conducted in concert with experimental studies by Jajja *et al*. [24], no heating data have been reported for sCO_2 convection in microchannels at high heat fluxes or with non-uniform heating. Some experimental heat transfer investigations have been performed in compact flow geometries, but these have been limited primarily to low-flux heat rejection applications relevant to refrigeration

and air-conditioning [25–33] (*i.e.*, supercritical gas coolers in transcritical vapor compression cycles). In these investigations, energy is removed from the boundary layer, and the flow physics are expected to be significantly different than in heat acquisition applications of interest. Refrigeration and air-conditioning applications typically do not present heat transfer deterioration or mixed convection type behavior. Thus, it is difficult to apply insights from supercritical cooling to heating applications.

Historically, computational modeling approaches have had limited reliability for supercritical transport phenomena, specifically in microscale geometires. The earliest computational studies in the 1950s – 1970s employed relatively simple turbulence models in 2D geometries [34–37]. In the 1980s and 1990s, numerical studies of supercritical flows still focused on 2D steady cases, employing RANS (using mixing length and $k-\varepsilon$ models) [38–40]. Advances in RANS modeling approaches, such as the shear-stress transport (SST) model of Menter [41], led to increased research activity in 2000s. Many recent studies have focused on comparing different RANS turbulence models for supercritical flows ([28,42,51–55,43–50]). While such studies can provide useful guidance for specific applications, the generality of findings from such studies is unclear. Recently, new RANS model formulations have been developed specifically to capture complex buoyancy-turbulence interactions in supercritical flows [56]. Due to the difficulty in capturing the effects of sharp property variations near pseudo-critical temperatures (T_{pc}), especially at high heat fluxes, no RANS-based methods have yet been demonstrated to be generally valid for supercritical convection.

In response to wide discrepancies between existing RANS-based turbulence studies of supercritical heat transfer, a number of investigators have recommended turbulence resolving approaches (Bae *et al.* [57,58], Yoo *et al.* [59], Azih [60], Licht *et al.* [61]). Direct numerical simulations (DNS) of supercritical turbulent flows in vertical round tubes (Bae *et al.* [57,58]) and horizontal round tubes (Chu and Laurien [62]) at low heat fluxes (< 10 W cm^{-2}) were performed. Pandey *et al.* [63] conducted DNS of supercritical turbulent channel flows under cooling conditions. However, the high computational requirements of such cases limited conditions to $Re_{D_H} < 10{,}000$. Recently, large eddy simulations (LES) have been performed by Niceno and Sharabi [64], also focused on uniformly-heated vertical pipe flow. LES studies generally require less computational resources than DNS studies. However, the high peak Prandtl number characteristic of supercritical flows ($Pr = 14$ for Niceno and Sharabi [64]), necessitated resolution of a very thin thermal boundary layer (down to y+ ~ 0.1). Findings from such studies indicate that supercritical turbulent flows have distinct phenomena from those found in subcritical flows employed to develop RANS models, such as high momentum ejections from the turbulent boundary layer due to buoyancy effects [58,59]. To the best of our knowledge, the only available numerical study on supercritical heat transfer at microchannel scale has been conducted by Asinari [44], using $k-\varepsilon$ RANS formulation, which was unable to accurately model transient effects happening in thermal boundary layer. Therefore, there is a need for conducting high-resolution simulations at microscale.

To date, no systematic investigation has been performed to characterize the transport mechanisms in microscale supercritical convection, specifically under non-uniform heating conditions. This work aims to address the following questions: (1) How applicable are published supercritical convection correlations for high-flux microchannel conditions? (2) What is the relationship between the Richardson number (Ri) and the onset of mixed convection in microchannels? (3) At fixed mass flux, how does increasing wall heat flux affect HTCs on walls with different orientations? (4) What is the impact of conjugate heat transfer between the fluid domain and solid channel walls in supercritical heat exchangers? Insights from this work can aid engineering of high-flux supercritical heat exchangers for advanced solar-thermal power generation and electronics cooling systems.

Following preliminary studies [65,66], this work is a part of a collaborative experimental and numerical investigation of high-flux heating of supercritical fluids in microscale geometries. A recent publication by our collaborators [24] presented experimental average HTC data for sCO_2 convection in microchannels at reduced pressures $P_r = 1.03 - 1.10$, mass fluxes $G = 200 - 1000$ kg m^{-2} s^{-1}, nominal heat fluxes $q'' = 20 - 40$ W cm^{-2}, and inlet temperatures $T_{f,in} = 20 - 100$ ℃ in a non-uniformly heated microchannel. Measurement of local flow patterns and property profiles were not feasible in those experiments. Local data from the present computational investigation can explain transport processes driving heat transfer trends observed in their study. After validating the simulation approach with experimental data from [24], the present investigation expands the range of heat flux to $q'' = 24 - 62$ W cm^{-2}, and focuses on conditions near the pseudo-critical temperature to resolve instability-driven unsteady phenomena and non-uniform heating effects that are challenging to measure experimentally. Furthermore, a representative conjugate heat transfer case study is simulated to evaluate the effect of interactions between solid microchannel wall and fluid domain on HTC performance.

2. Simulation Approach

2.1. Governing Equations

A pseudo-incompressible LES simulation scheme is employed to study the turbulent supercritical microchannel convection processes in this investigation. The governing continuity, momentum, and energy equations for velocity (u), pressure (p), and enthalpy (h) fields are:

$$\frac{\partial \rho}{\partial t} + \frac{\partial}{\partial x_i}(\rho u_i) = 0 \tag{1}$$

$$\frac{\partial (\rho u_i)}{\partial t} + \frac{\partial}{\partial x_j}\left(\rho u_j u_i\right) = -\frac{\partial p}{\partial x_i} + \frac{\partial}{\partial x_j}\left[(\mu + \mu_{\mathrm{SGS}})\frac{\partial u_i}{\partial x_j}\right] + \rho g_i + \overrightarrow{F_B} \tag{2}$$

$$\frac{\partial (\rho h)}{\partial t} + \frac{\partial}{\partial x_i}(\rho u_i h) = \frac{\partial}{\partial x_j}\left[(\alpha + \alpha_{\mathrm{SGS}})\frac{\partial h_i}{\partial x_j}\right] \tag{3}$$

where, μ_{SGS} and α_{SGS} stand for the modeled LES sub-grid scale (SGS) contributions. The wall-adapting local eddy-viscosity (WALE) LES model [67] is employed. A constant turbulent Prandtl number of $Pr_t = 0.85$ is used. Thermophysical properties of the supercritical carbon dioxide (ρ, c_p, μ, k) are evaluated using explicit formulations

for sCO_2 density (Peng-Robinson equation of state [68]) and curve fits for specific heat capacity (c_p), Prandtl number (Pr), and dynamic viscosity (μ) (see Appendix A). The average absolute deviations (AAD) of the property values from curve fits for $c_p, \mu,$ and Pr are 6%, 1%, and 2%, respectively with data from [69,70]. To set the mass flux in the channel, a body-force term $(\vec{F}_B)$ is added to the momentum equation (Eqn. 2), which represents the mean pressure gradient. At each time step, the magnitude of mass flux ($G = \rho U$) in the channel is calculated and compared with the target value. Based on the offset from the target value, $\vec{F}_B$ is adjusted and the velocity field is corrected.

2.2. Solver Algorithm

Simulations are performed using a modified version of a velocity-pressure-enthalpy coupled unsteady pseudo-incompressible flow solver in OpenFOAM v1612+ [71] (buoyantPimpleFoam), which adjusts $\vec{F}_B$ to maintain a constant mass flux. The *pseudo-incompressible* assumption is that density only varies with temperature, as variations in pressure are small relative to the mean pressure.

A second order implicit discretization scheme is used for time stepping and a third-order interpolation scheme is adopted for gradient terms. The divergence and Laplacian terms are discretized with second order linear interpolation schemes. Therefore, the simulations theoretically have second-order accuracy.

2.3. Studied Geometry and Boundary Conditions

The simulation domain is designed to correspond to the experimental test section of [24]. That test section had 750 µm × 737 µm channels with 30 mm long upstream unheated sections for turbulent flow development and 20 mm long bottom-heated downstream sections. To reduce the computational costs, the simulation geometry

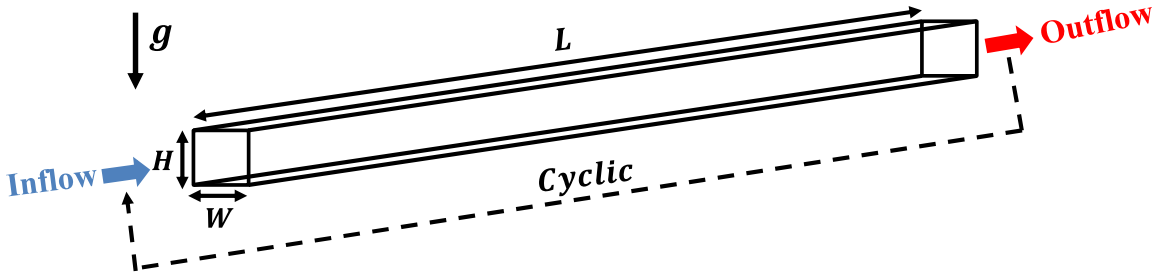

Figure 2. Schematic of the simulation geometry

Table 1. Dimensions of the computational domain

Section	Size
Channel Width (W)	750.02 µm
Channel Height (H)	737.32 µm
Channel Length (L)	5 mm

consists of a cyclic 5 mm long 750 μm × 737 μm cross section channel, corresponding to a portion of the fully-developed heated region of the experimental test-section. The schematic of the simulation geometry is presented in Fig. 2, and corresponding dimensions are listed in Table 1.

The error introduced by approximating the 20 mm downstream heated section with a 5 mm cyclic domain can be estimated using results for turbulent channel flow with an unheated starting length [72]. Essentially, this is the error introduced by approximating the heated region as a very long or cyclic region. In the heated region (0 to x^*), the ratio between the average heat transfer coefficient and that for thermally fully developed flow at the same Re is, to first order:

$$\frac{\mathrm{Nu}_m}{\mathrm{Nu}_\infty} = 1 + \frac{1}{x^* \lambda_0^2} ln \frac{\lambda_0^2}{8 G_0} \tag{4}$$

For $\mathrm{Pr} = 8$ and $\mathrm{Re} = 50{,}000$ (comparable to our studied conditions), $\lambda_0^2 = 685.6$, $G_0 = 85.4$ [72]. For the studied test section, $x^* = (2x/D_H)/(\mathrm{Re\ Pr}) = (2 \cdot 20\ \mathrm{mm}/0.75\ \mathrm{mm})/(50{,}000 \cdot 8) = 1.33 \cdot 10^{-4}$. Substituting these values into the above expression yields $\mathrm{Nu}_m/\mathrm{Nu}_\infty$ = 1.038. This suggests that approximating the heated region with a cyclic flow condition (*i.e.*, assuming it is very long) may introduce an approximately 4% error in the HTC, which is acceptable for turbulent flow simulations.

A second limitation of this cyclic simulation approach is that it does not capture axial property variations (particulary density) that are present in long heated channels. Appendix B presents a comparison between cyclic and full-length (non-cyclic) implementations of a representative case. Average HTCs match within ~3% between the two implementations, indicating that axial property variations introduce relatively minor effects on heat transfer for these conditions.

Prior relevant wall-bounded LES modeling studies, which consider the effect of Prandtl number on the required mesh resolution, were consulted to design the computational mesh structure [73,74]. Based on recommendations from these studies, the mesh is configured so that near-wall first-cell $x^+ = 0.26$ and $y^+ = 0.26$, with stretching factors of $1.03 - 1.06$ in x and y directions (normal to the walls). The computational grids are uniformly spaced in the flow direction, with $z^+ = 9.4 - 199.2$, depending on the studied Re and wall heat flux.

At inlet and outlet of the channel, a cyclic boundary condition is employed for all the fields, which represents tracking a volume of fluid as it is heated along the flow direction. The pressure gradient in the channel was decomposed into two parts, *i.e.*, $\nabla p = \nabla \overline{p} + \nabla p'$. Here, $\nabla \overline{p}$ is the mean pressure gradient that enforces the desired mass flux, and is applied through $\overrightarrow{F_B}$ (c.f. Section 2.1). $\nabla p'$ is due to local turbulent pressure fluctuations, and has zero mean value. This decomposition allowed the pressure field to be compatible with cyclic boundary condition. This cyclic approach allows evaluation of HTC values for a range of bulk fluid temperatures in each simulation. No-slip velocity boundary conditions are applied on all the channel walls. A zero-mass-flux pressure boundary condition is applied on all the channel walls.

One objective of this investigation is to study non-uniform supercritical convection heat transfer on micro-channel heat exchanger surfaces. This can occur due to: (1) mixed convection from gravity-induced stratification

degrading heat transfer on downward-facing heated surfaces, and (2) conjugate heat transfer resulting in different average temperatures on top/bottom and side walls. A preliminary simulation was conducted to determine whether supercritical convection on different walls in a microchannel could be assumed independent. To clarify this concept, consider a channel with bottom, side, and top-wall temperatures T_B, T_S, T_T and temperature values T_1, T_2, T_3. Convection on different surfaces could be argued to be independent if the measured heat transfer coefficient on a given surface at a given temperature does not depend on the other surface temperatures (*e.g.*, $h_B(T_B = T_1, T_S = T_2, T_T = T_3) \approx h_B(T_B = T_1, T_S = T_1, T_T = T_1)$). A representative set of test cases with a mass flux of $G = 1000\ \mathrm{kg\ m^{-2}\ s^{-1}}$ were evaluated to assess whether convection from different microchannel surfaces could be assumed independent in this investigation. In the first case, all walls were set to be isothermal (329.7 K) and time- and space-averaged heat flux values were collected for each wall. In the other cases, the microchannel was only heated from one side (*i.e.*, top, bottom, or side walls set to 329.7 K) and zero heat flux boundary conditions were imposed on the other sides. Wall heat flux values were compared from the all-wall case and from heated walls in the single-wall heated cases, and the average absolute deviation (AAD= $\left|\frac{HTC_{sim,avg} - HTC_{corr,HTC}}{HTC_{corr,HTC}}\right|_{avg}$) for heat transfer coefficients between the pairs were less than 4.1%. This indicates that, for conditions studied here, convection on different walls can be assumed independent, and a single simulation with isothermal channel walls can yield accurate heat transfer predictions for upward-facing, downward-facing, and vertical microchannel surfaces at that temperature. Isothermal wall boundary conditions are therefore used for the majority of cases in this study to limit computational costs (except for validation and CHT cases).

3. Results and Discussion

Following a grid independence study (discussed in section 3.1, below) and a validation study with experimental data of [24], twelve cases are simulated at reduced pressure of $P_r = 1.1$, varying mass flux $G = 100 - 1000\ \mathrm{kg\ m^{-2}\ s^{-1}}$, and varying average heat flux $q'' = 24 - 62\ \mathrm{W\ cm^{-2}}$. Three mesh resolutions are evaluated for each case to obtain Richardson-extrapolated heat flux values and estimated uncertainties. Heat transfer results are then compared with available supercritical convection correlations (Liao and Zhao [75]; Petukhov et al. [76]; and Jackson and Hall [77]) as well as the conventional turbulent single-phase channel flow heat transfer correlation of Dittus-Boelter [78] to assess validity of these models for engineering supercritical microchannel heat exchangers. Transient wall heat flux data are separately collected for each side (*i.e.*, top, bottom, and side walls) to form a criterion for the onset of supercritical mixed convection. Finally, a conjugate heat transfer case (microchannel in a stainless steel heat exchanger) is studied to assess the impact of non-uniform heat transfer coefficients in practical heat exchanger applications.

3.1. Grid Sensitivity and Validation Study

A grid sensitivity study was first performed to verify that the simulation and meshing approach is convergent. A representative case was selected with reduced pressure of $P_r = 1.1$, mass flux $G = 1000\ \text{kg m}^{-2}\ \text{s}^{-1}$ ($\text{Re}_{D_H} = 22{,}410$), and inlet temperature $T_{in} = 26.9\ ℃$. Five meshes were evaluated (Course, Medium, Fine, Finer, and XFine) with a refinement factor between meshes of 1.4 in every direction ($x, y,$ and z) as suggested by [79] (details in Table 2). All cases were conducted with uniform temperatures for all the wall boundaries, where $T_w - T_{f,in} = 8.9\ ℃$. Simulations results were logged beginning 15 flow cycles after quasi-steady flow behavior was observed. The plot of average wall heat flux values (average of the all four sides) as a function of time is shown in Fig. 3. Convergence was observed by the Finer case (q''_{avg} is within $\pm 1\%$ from XFine case), indicating that no further grid refinement was necessary. Based on the results from the Medium, Fine, and Finer grids, the empirical rate of convergence for average wall heat flux is approximately second order (p = 1.73), as expected. Representative velocity and temperature fields from this case are shown in Fig. 4, below. At this high mass flux condition, nearly identical veloctity and temperature profiles were observed near all four walls, suggesting negligible mixed convection effects (detailed discussion in Section 3.3).

Using the method suggested by [79], the results of three mesh resolutions are used to obtain Richardson-extrapolated curves and uncertainties for average wall heat flux for each case in this paper.

Table 2. Summary of mesh independence study case design

Re	**Case**	**No. of mesh elements ($x \times y \times z$)**
22,410	Course	373,248 (72×72×72)
	Medium	1,000,000 (100×100×100)
	Fine	2,744,000 (140×140×140)
	Finer	7,529,536 (196×196×196)
	XFine	20,570,824 (274×274×274)

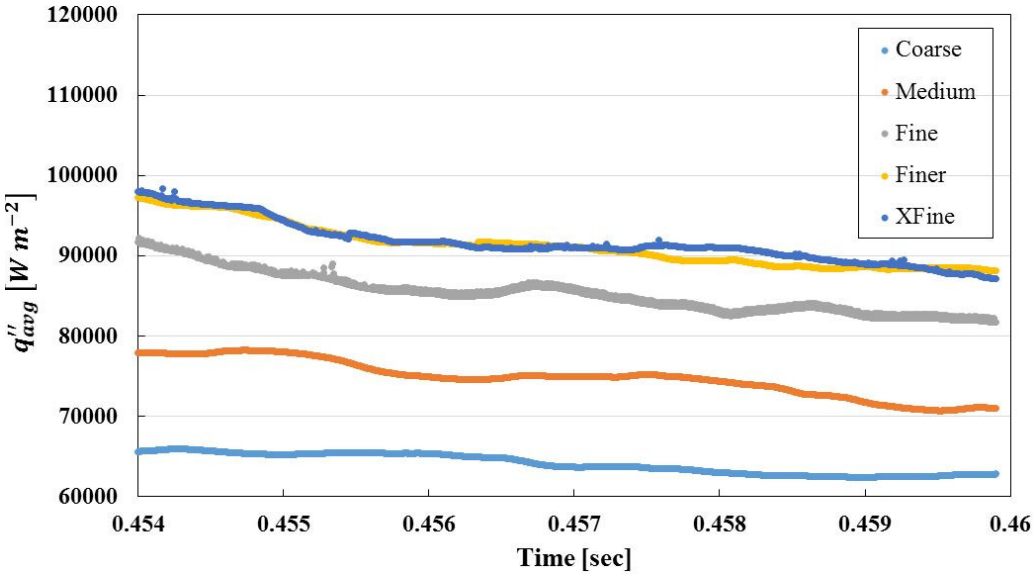

Figure 3. Average wall heat flux vs. time for the grid sensitivity study

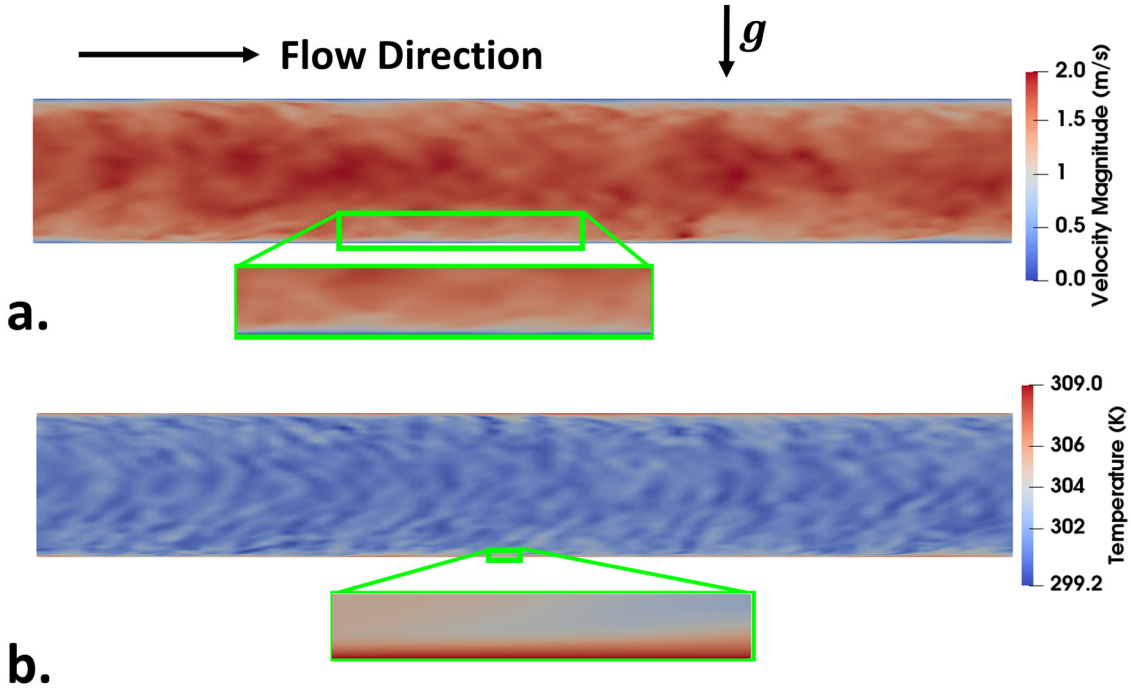

Figure 4. Simulation results for grid convergence study. a. Cross-section velocity magnitude, with detail view of velocity boundary layer. b. Channel cross-section temperature field with detail view of thermal boundary layer (lower 5% of channel).

To validate the approach, two separate test cases simulated. First, a constant-property turbulent channel flow study was performed to assess validity of the underlying approach, independnent of effects due to supercritical

property variations. Wall heat flux and frictional pressure drop gradient data from this case can be compared with the widely accepted correlation predictions of Gnielinski [80]. In this study, the constant fluid properties were set to those of CO_2 at reduced pressure of $P_r = 1.1$ and $= 314$ K $\left(\rho = 281.3\ kg\ m^{-3}, c_p = 4{,}910\ J\ kg^{-1}\ K^{-1},\ \mu = 2.254 \times 10^{-5}\ kg\ m^{-1}\ s^{-1}, \mathrm{Pr} = 2.598\right)$. The mass flux was set to $G = 300$ kg m^{-2} s^{-1} ($\mathrm{Re}_{D_H} = 9{,}900$), the wall temperatures were set to $T_w = 318$ K , and the fluid was initialized at $T = 314$ K. The simulation geometry was the same as described in section 2.3 (see Fig. 2) with cyclic inlet and oulet boundary conditions. Following the methodology discussed in the grid sensitivity study, three mesh cases (Medium, Fine, and Finer) were simulated. Then, Richardson-extrapolated curves and uncertainties for average wall heat flux and channel pressure drop were compared with the Gnielinski [80] correlations (Fig. 5). Simulation results for average wall heat flux and pressure drop were $q''_{sim,avg} = 15{,}700 \pm 1{,}300$ W m^{-2} and $\Delta P_{sim,avg} = 39.3 \pm 4.6$ Pa. These values match the predictions of the Gnielinski correlation [80] within uncertainty $\left(q''_{\mathrm{Gn},avg} = 15{,}284\ \mathrm{W\ m^{-2}},\ AAD_{q'',Gn} = 3.2\%,\right.$ and $\left.\Delta P_{\mathrm{Gn,avg}} = 42.1\ \mathrm{Pa}, AAD_{\Delta P,Gn} = 6.6\%\right)$

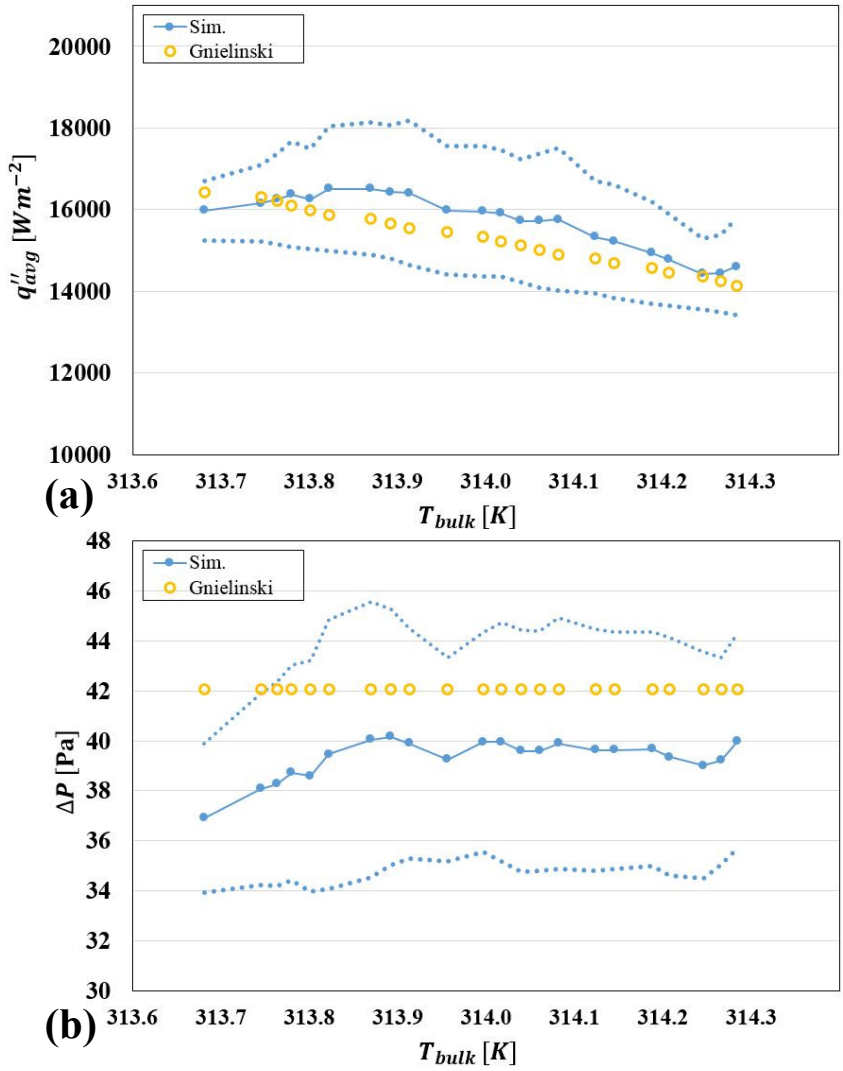

Figure 5. Results of constant-property LES simulation validation study compared with the Gnielinski correlation [80] for (a) averaged wall heat flux (q''_{avg}), and (b) microchannel pressure drop (ΔP). The numerical uncertainty range is shown in dotted light blue.

In a second validation test accounting for temperature dependent properties, a representative case was evaluated with reduced pressure of $P_r = 1.1$, mass flux of $G = 500\ \text{kg m}^{-2}\ \text{s}^{-1}$, and flow inlet temperature of of $T_{f,in} = 28.9\ ^{\circ}\text{C}$, which corresponds to an experimental case studied by [24]. The experimental test section of [24] consisted of five microchannels of 750 µm × 737 µm cross section, and 50 mm length (Fig. 6). The upstream 30 mm of the test section was not directly heated to permit hydrodynamic development. The downstream 20 mm of flow length was heated from the bottom through a stainless steel boss. All other faces of the test section were insulated. Six temperature sensors were embedded in the heated block to determine heat flux and extrapolate

channel wall temperatures. The computational domain in the proposed LES study is a cyclic 5 mm-long channel, which is intended to represent a portion of the directly-heated experimental test-section channels.

While the major portion of input heat in the experimental test section of [24] reached the downstream 20 mm of the channels, a portion was conducted upstream. An inverse heat transfer study was performed here to determine the specific boundary conditions in the directly heated portions of the channels and facilitate comparison between simulation and experimental data. A simplified 1D-3D modeling approach was used for this inverse study (in COMSOL Multiphysics® v. 5.3 [81]). The overall dimensions of the 1D-3D computational geometry were the same as the experimental test section (Fig. 6). The sCO_2 fluid channels were modeled as 1D flow, with no axial conduction and well-mixed at each cross-section (Fig. 7). The sides and top of the metal block are insulated in this computational study (zero-gradient temperature boundary condition) to replicate experimental conditions. Tabulated sCO_2 thermo-physical properties were used [69,70]. Six temperature probes were defined at the same locations as in the the experiments. A parametric study was performed for average channel HTC (10 cases with $h_{\text{avg}} = 4900 - 7940$ W m^{-2} K^{-1}) to find the value that minimized RMS temperature probe error with experiments (Eqn. 5).

$$P = \sqrt{\sum_{i=1}^{6}\left(T_{sim} - T_{exp,flux\ meters}\right)^2}/6 \tag{5}$$

The minimum value for the temperature error fuction was $P = 1.15$℃ corresponding to $h_{avg} = 6920$ W m^{-2} K^{-1}. While the actual heat transfer coefficient is expected to vary over the channel surfaces, it is challenging to inversely estimate the distribution as only local temperatures were experimentally measured at the channel inlets and outlets and in the heated block.

The average wall temperature values for the heated section of the microchannels in the 1D-3D inverse study were then calculated separately for the bottom, top, and side walls $\left(T_{\text{bot,avg}} = 325.4\text{ K}, T_{\text{side,avg}} = 323.2\text{ K}, T_{\text{top,avg}} = 321.8\text{ K}, T_{\text{bulk,avg}} = 311.9\text{ K}\right)$. These values were then imposed as constant temperature boundary conditions on the walls of the cyclic 5 mm channel domain in the LES simulations. Three mesh resolutions were solved to obtain Richardson-extrapolated curves for average heat transfer coefficients (HTCs) on different walls. Heat transfer coefficients were calculated for each time step as: $HTC = q_w''/(T_w - T_{bulk})$. Here, q_w'' and T_w are the area averaged heat flux and temperature, respectively, on the considered walls. The bulk fluid temperature is defined based on the mass-flow-weighted average enthalpy: $T_{bulk} = T(\bar{h}, p)$ where $\bar{h} = (\int_\forall \rho h u\, d\forall)/(\int_\forall \rho u\, d\forall)$ over the domain volume ($\forall$). Instantaneous HTC curves from simulations were compared with the experimental value of 6920 W m^{-2} K^{-1}. The plot of average HTC value from the inverse analysis of experimental data compared with the Richardson-extrapolated HTC curves for different walls based on LES simulations is shown in Fig. 9. The timed-averaged HTC values and uncertainties are reported in Table 3. The AAD of the computationally predicted average HTCs from the validation study compared to the experimental value ranges from $\pm 4.8\%$ for the bottom wall to $\pm 23.9\%$ for the top wall. This reasonable agreement indicates

validity of the employed LES approach. It should be noted that based on mixed-convection physics, the lower wall HTC should be greater than the side walls. Therefore, the uniform HTC extracted from the inverse study probably over-estimates the top wall and underestimates the bottom wall, suggesting even closer agreement with simulations.

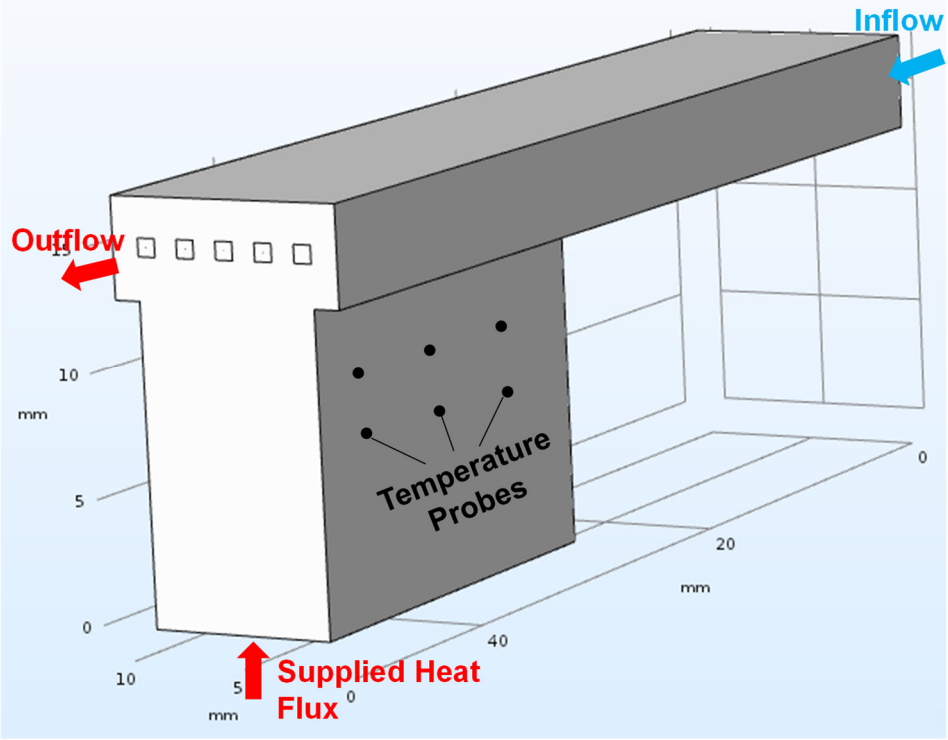

Figure 6. Schematic of the experimental test section

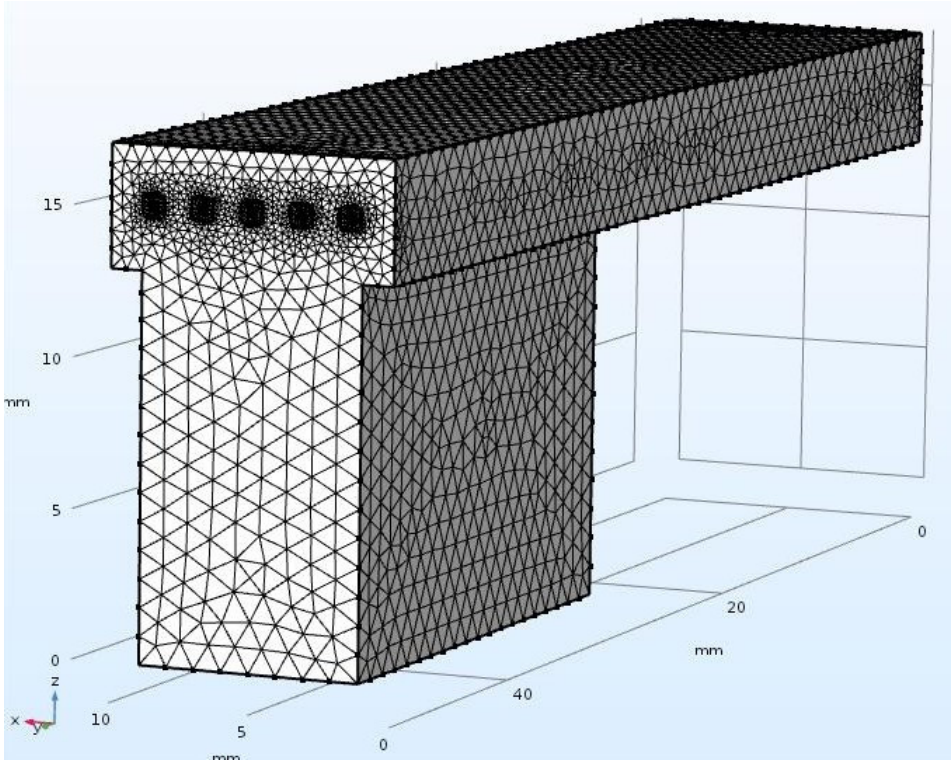

Figure 7. Mesh structure of the computational domain for the inverse study

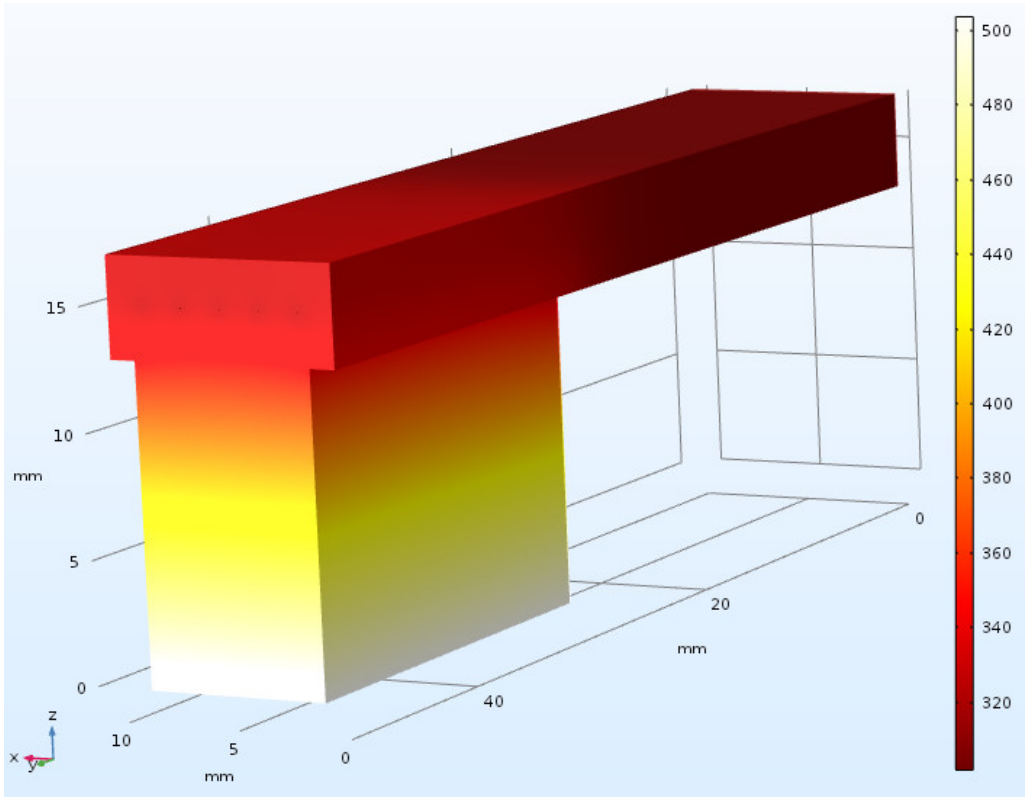

Figure 8. Steady state temperature profile in the inverse study computational domain, (units of K)

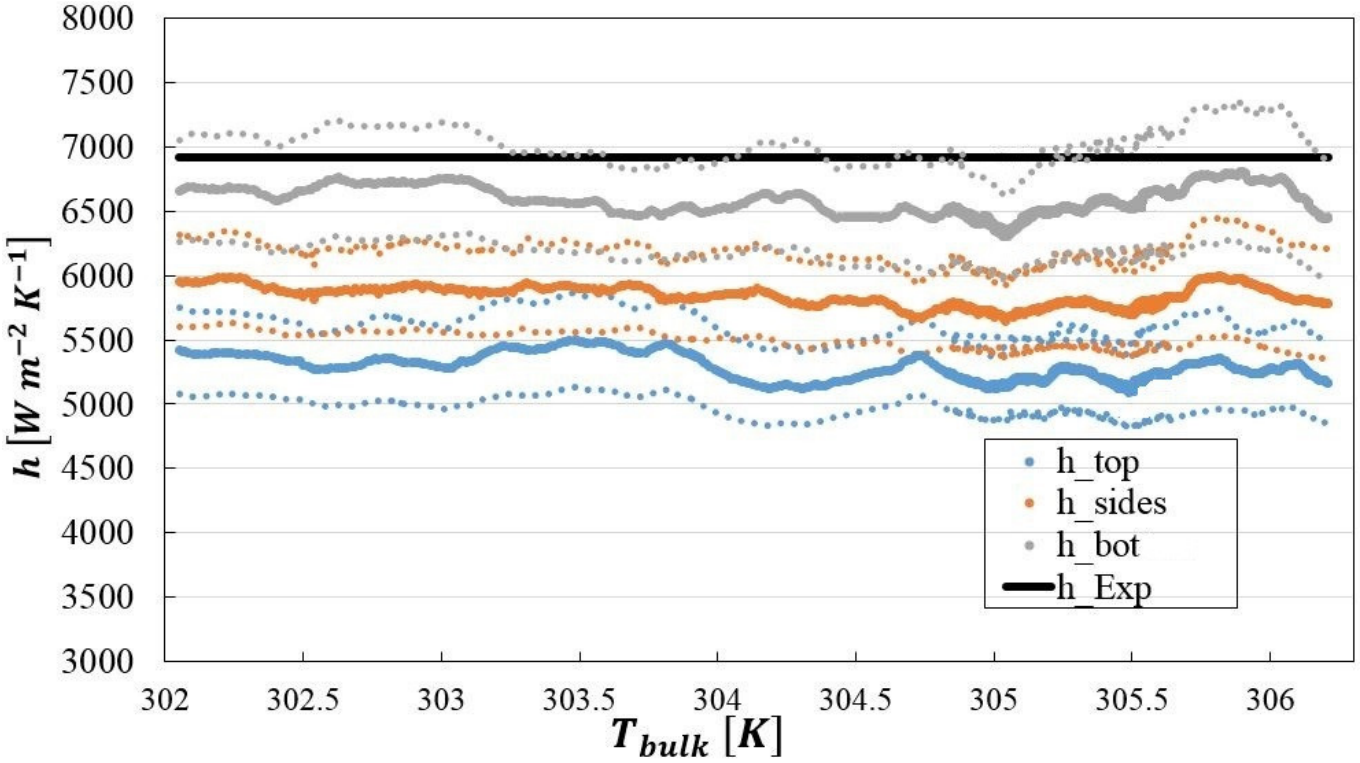

Figure 9. Average experimental HTC compared with the simulation predictions for different walls as a function of bulk fluid temperature. Dashed lines correspond to the lower and upper HTC bounds considering numerical uncertainties

Table 3. Average heat transfer predictions from the simulation study compared with values estimated through inverse analysis of experimental data

HTC	Avg. Value $\pm$ Uncertainty [W $m^{-2}K^{-1}$]
$h_{\text{avg,exp}}$ (from inverse heat transfer analysis)	6920 ± 160
$h_{\text{bot,avg,sim}}$	5270 ± 430
$h_{\text{sides,avg,sim}}$	5830 ± 320
$h_{\text{top,avg,sim}}$	6590 ± 360

3.2. Assessment of Available Convection Correlations for Supercritical CO_2 Heat Transfer at Pseudocritical Conditions in Microchannels

A parametric study was conducted to characterize supercritical CO_2 microchannel convection phenomena and assess the validity of supercritical convection correlations (Petukhov *et al.* [76]; Jackson and Hall [77]; and Liao and Zhao [75]) and the constant-property correlation of Dittus-Boelter [78]. Values predicted with these correlations are denoted with subscripts *P*, *JH*, *LZ*, and *DB*, respectively. Simulations were conducted at four mass flux values ranging over $G = 100 - 1000$ kg m^{-2} s^{-1} (Re $= 3{,}000 - 36{,}000$), where Re $= \frac{GD_H}{\mu}$, with channel hydraulic diameter of $D_H = 743.6\ \mu m$ and the reference value for μ is calculated at bulk fluid temperature. For each mass flux, simulations were performed at three different average wall heat flux values. The range of studied T_{bulk} values is listed in Table 4, and shown schematically in Fig. 10. Bands of ±5 K are indicated around the pseudocritical temperature (T_{pc}). Sharp property variations with temperature occur in this range. The test cases are selected such that for the majority, $T_{bulk} < T_{pc} < T_w$. For such conditions, significant property variations occur across the boundary layers, which can yield strong heat transfer deterioration and mixed convection effects [10,11,82].

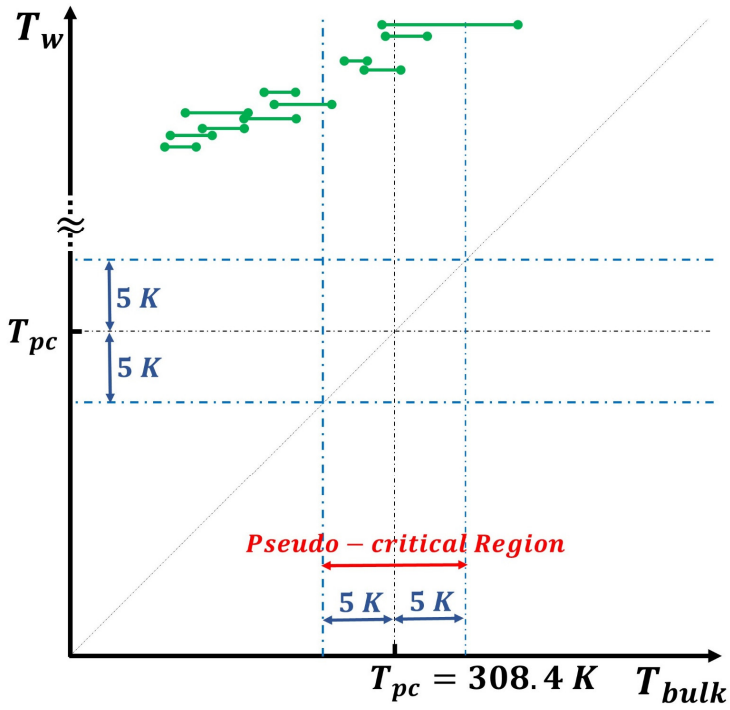

Figure 10. Schematic representation of studied temperature range (highlighted in green)

Table 4. Summary of the studied range of T_{bulk} and T_w along with reference property values

Case	$G\ [kg\ m^{-2}\ s^{-1}]$	Re $[-]$	$U_{avg}\ [m\ s^{-1}]$	$\rho\ [kg\ m^{-3}]$	$\mu\ [kg\ m^{-1}\ s^{-1}]$	$T_w\ [K]$	$T_{bulk}\ [K]$
1	100	3,000	0.29 – 0.34	258 – 517	$2.17 \times 10^{-5} - 3.71 \times 10^{-5}$	495.5	308.0 – 316.8
2	100	3,200	0.31 – 0.32	345 – 505	$2.55 \times 10^{-5} - 3.61 \times 10^{-5}$	460.5	308.0 – 310.3
3	100	3,400	0.32 – 0.34	442 – 621	$3.14 \times 10^{-5} - 4.67 \times 10^{-5}$	420.5	306.4 – 308.6
4	300	10,000	0.99 – 1.03	587 – 653	$4.33 \times 10^{-5} - 5.02 \times 10^{-5}$	425.5	305.5 – 306.7
5	300	11,000	1.17 – 1.26	693 – 765	$5.50 \times 10^{-5} - 6.50 \times 10^{-5}$	376.5	299.4 – 303.9
6	300	11,100	1.23 – 1.29	735 – 779	$6.06 \times 10^{-5} - 6.71 \times 10^{-5}$	356.5	298.2 – 300.4
7	500	17,500	1.96 – 2.03	745 – 781	$6.20 \times 10^{-5} - 6.74 \times 10^{-5}$	392.5	298.1 – 300.9
8	500	18,300	2.12 – 2.18	776 – 802	$6.68 \times 10^{-5} - 7.10 \times 10^{-5}$	355.5	296.1 – 298.4
9	500	18,300	2.17 – 2.24	797 – 823	$7.01 \times 10^{-5} - 7.49 \times 10^{-5}$	335.5	293.9 – 296.6
10	1,000	34,200	4.22 – 4.31	831 – 846	$7.64 \times 10^{-5} - 7.93 \times 10^{-5}$	319.7	291.3 – 293.0
11	1,000	35,700	4.37 – 4.47	824 – 841	$7.50 \times 10^{-5} - 7.83 \times 10^{-5}$	329.7	291.9 – 293.8
12	1,000	35,700	4.21 – 4.46	795 – 839	$6.97 \times 10^{-5} - 7.78 \times 10^{-5}$	359.7	292.4 – 296.8

3.2.1. $G = 100\ kg\ m^{-2}\ s^{-1}$

At this mass flux, three values of average wall heat flux in the range of of $q''_{avg} = 27 - 37\ \text{W cm}^{-2}$ were studied. These simulations correspond to high-heat-flux low Reynolds number turbulent flow ($\text{Re} = 3{,}000 - 3{,}400$). For the $q''_{avg} = 37\ \text{W cm}^{-2}$ case, the maximum temperature difference reached $T_w - T_{f,in} = 206.1$ K. Therefore, no higher flux cases were evaluated. Simulation values for average HTC (and uncertainty) vs. bulk flow temperature for these cases are compared with published supercritical correlations [75–77] and the Dittus-Boelter constant property model [78] in Fig. 11. Time-averaged HTC values as well as AAD and logarithmic scale deviation (LSD) between numerical results and each correlation are tabulated in Table 5. LSD is defined as:

$$LSD = \left| \log_{10} \left(\frac{\text{HTC}_{\text{sim,avg}}}{\text{HTC}_{\text{corr,avg}}} \right) \right| \tag{6}$$

In this low Re – high heat flux regime, the Dittus-Boelter [78] model shows closest agreement with simulations ($AAD_{max} = 24\%$). The supercritical correlations differ by $AAD = 99\% - 268\%$, regardless of wall heat flux.

As heat flux increases, HTC at the microchannel wall decreases in this low Re – high heat flux flow regime. Of the three supercritical models, only the correlation of Petukhov *et al.* [76] shows a decreasing trend of HTC as T_{bulk} approaches T_{pc} (see Fig. 11(a)), as well as when T_{bulk} exceeds T_{pc} (see Figs. 10(b) and (c)). This trend is compatible with the simulation predictions. The model of Dittus-Boelter [78] in all the cases, predicts a local peak in HTC where $T_{bulk} \cong T_{pc}$.

Table 5. Time-averaged LES simulation HTC values and correlations values for $G = 100$ kg m^{-2} s^{-1}

$q''_{avg}[W\ cm^{-2}]$ $q''_{bot}[W\ cm^{-2}]$ $q''_{sides}[W\ cm^{-2}]$ $q''_{top}[W\ cm^{-2}]$	$T_w\ [K]$	$Re\ [-]$	HTC_{sim} $[W\ m^{-2}K^{-1}]$	HTC_P [76] $[W\ m^{-2}K^{-1}]$ (AAD, LSD)	HTC_{JH} [77] $[W\ m^{-2}K^{-1}]$ (AAD, LSD)	HTC_{LZ} [75] $[W\ m^{-2}K^{-1}]$ (AAD, LSD)	HTC_{DB} [78] $[W\ m^{-2}K^{-1}]$ (AAD, LSD)
27 35 28 17	420.5	3,400	2,384	1,140 (112% , 0.32)	654 (268% , 0.56)	1,191 (103% , 0.30)	2,743 (24% , 0.06)
34 46 35 19	460.5	3,200	2,229	789 (184% , 0.45)	622 (258% , 0.55)	1,119 (99% , 0.30)	2,922 (23% , 0.12)
37 53 37 21	495.5	3,000	1,992	710 (183% , 0.45)	554 (257% , 0.56)	954 (108% , 0.32)	2,325 (21% , 0.07)

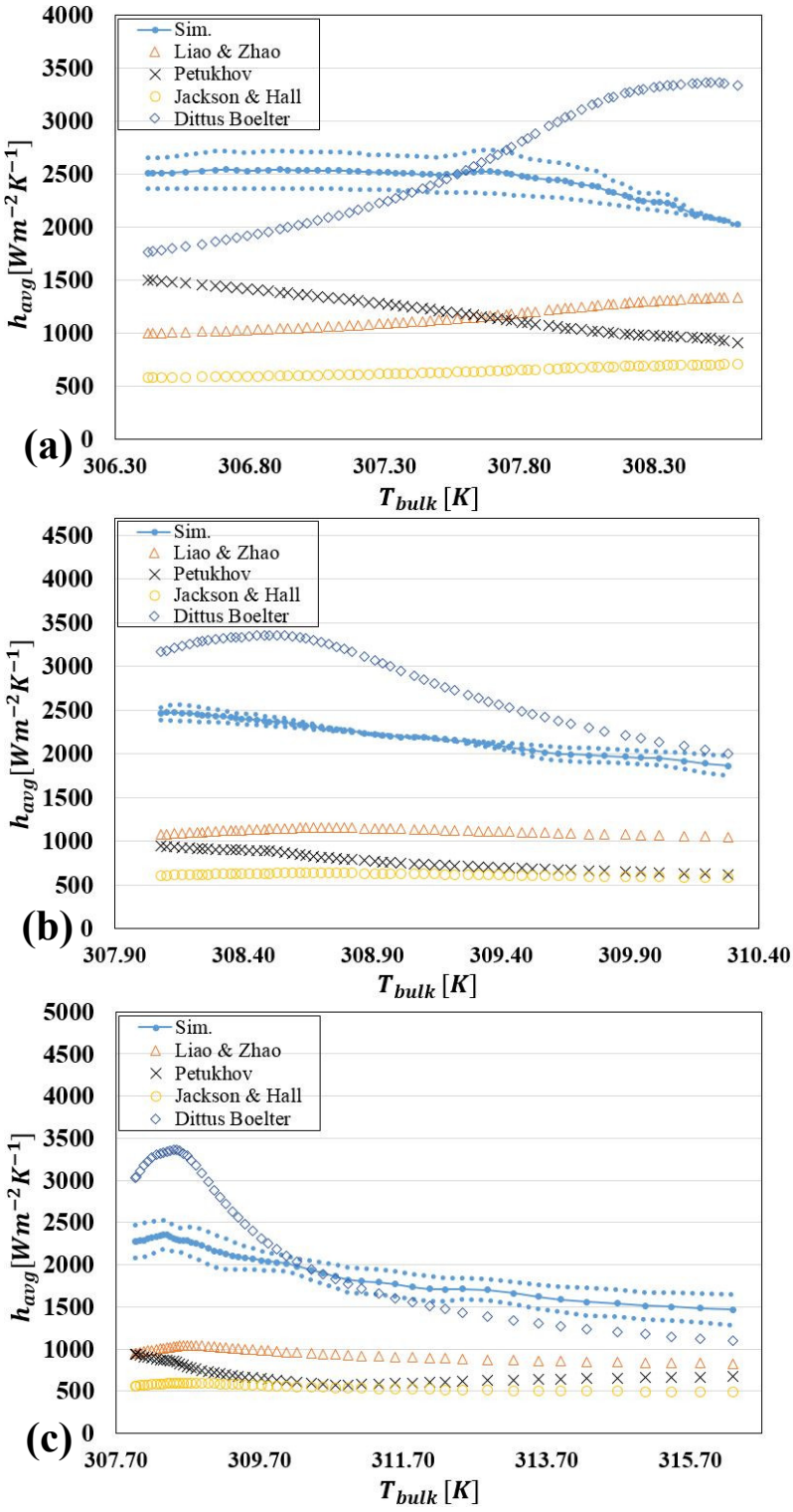

Figure 11. Average LES simulation and correlation HTC values vs. bulk fluid temperature for $G = 100$ kg $\mathrm{m^{-2}\ s^{-1}}$, and (a) $q''_{avg} = 27$ W $\mathrm{cm^{-2}}$, (b) $q''_{avg} = 34$ W $\mathrm{cm^{-2}}$, and (c) $q''_{avg} = 37$ W $\mathrm{cm^{-2}}$. The numerical uncertainty range is shown in dotted light blue.

3.2.2. $G = 300\ kg\ m^{-2}\ s^{-1}$

Three cases were evaluated at G = 300 kg m^{-2} s^{-1} ($\mathrm{Re} = 10{,}000 - 11{,}100$) and average wall heat fluxes ranging over $q''_{avg} = 25 - 62$ W cm^{-2}. Plots of average HTCs and uncertainties vs. bulk flow temperature are presented and compared with correlations in Fig. 12. Average HTC values are also tabulated in Table 6. At this mass flux, as heat flux increases, simulation HTCs increase slightly, opposite of results for the low Re – high flux cases. Overall, the predictions of Dittus-Boelter [78] are reasonably close to the simulation values ($AAD_{max} = 67\%$), and the deviation decreases as wall heat flux increases. At higher heat fluxes, near-wall temperatures are well above $T_{\mathrm{pc}} = 308.4$ K while $T_{bulk} < T_{pc}$ for all cases. Of the supercritical correlations, only the model of [76] shows relatively close agreement, and only at lowest heat flux ($AAD = 45\%$). The AAD of all supercritical correlations increase with increasing heat flux.

In this intermediate Re – high flux regime, the simulations and correlations predict low sensitivity of HTC to q''_{avg}, even for cases with $q''_{avg} = 35$ W cm^{-2}, 62 W cm^{-2}, in which T_{bulk} approaches T_{pc}.

Table 6. Time-averaged LES simulation HTC values and correlations values for $G = 300$ kg m^{-2} s^{-1}

$q''_{avg}[W\ cm^{-2}]$ $q''_{bot}[W\ cm^{-2}]$ $q''_{sides}[W\ cm^{-2}]$ $q''_{top}[W\ cm^{-2}]$	$T_w\ [K]$	$Re\ [-]$	HTC_{sim} $[W\ m^{-2}K^{-1}]$	HTC_P [76] $[W\ m^{-2}K^{-1}]$ (AAD, LSD)	HTC_{JH} [77] $[W\ m^{-2}K^{-1}]$ (AAD, LSD)	HTC_{LZ} [75] $[W\ m^{-2}K^{-1}]$ (AAD, LSD)	HTC_{DB} [78] $[W\ m^{-2}K^{-1}]$ (AAD, LSD)
25	356.5	11,000	4,416	3,042	1,792	2,018	2,649
25				(45% , 0.16)	(146% , 0.39)	(119% , 0.34)	(67% , 0.22)
26							
24							
35	376.5	11,000	4,680	2,518	1,601	1,753	2,871
37				(86% , 0.27)	(192% , 0.47)	(167% , 0.43)	(63% , 0.21)
34							
33							
62	425.5	10,000	5,219	1,648	1,390	1,474	3,985
65				(217% , 0.50)	(276% , 0.57)	(254% , 0.55)	(31% , 0.12)
62							
59							

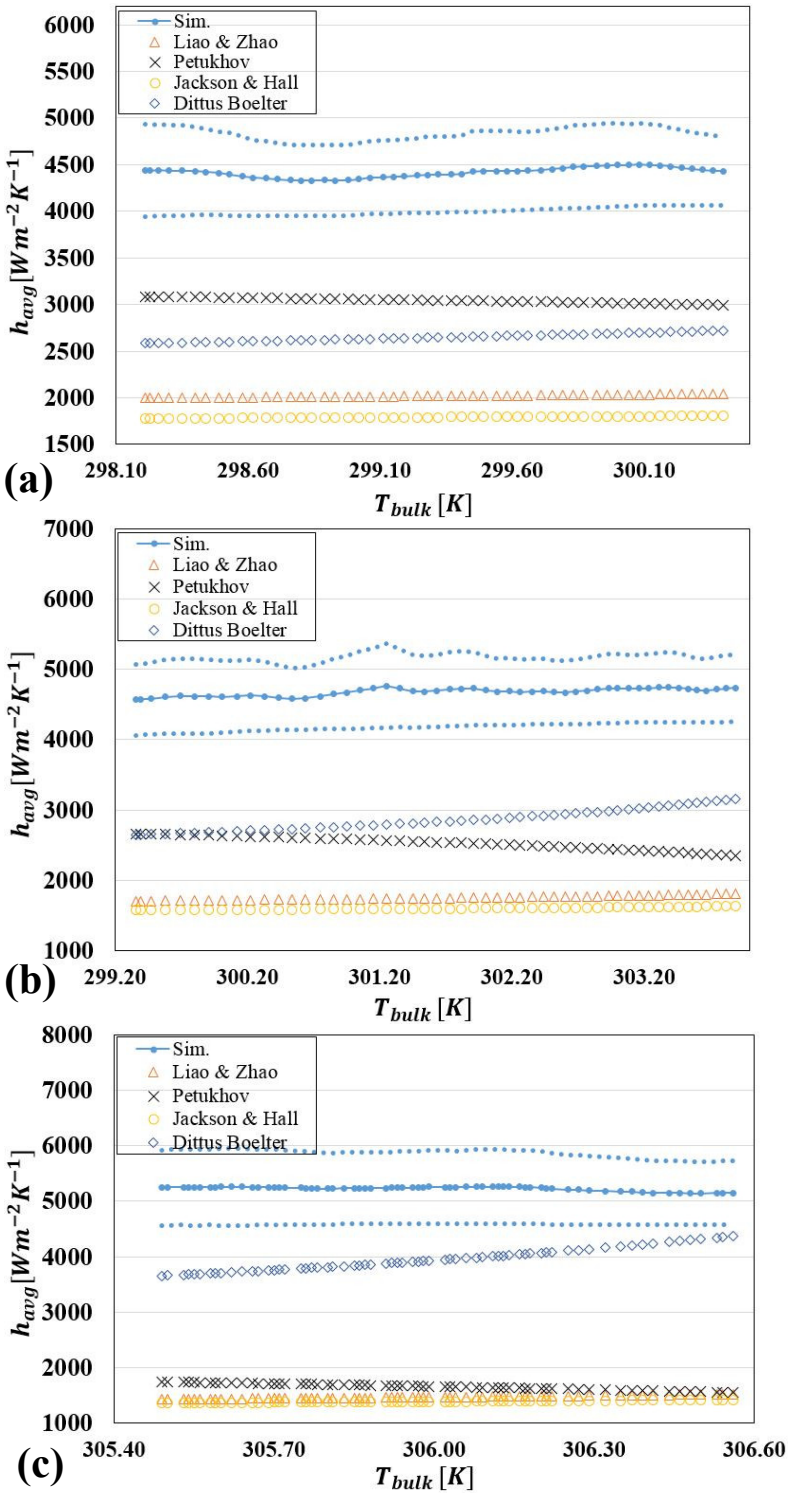

Figure 12. Average simulation HTC values vs. bulk fluid temperature compared with correlations for $G = 300$ kg $\mathrm{m^{-2}\ s^{-1}}$, and (a) $q''_{avg} = 25$ W $\mathrm{cm^{-2}}$, (b) $q''_{avg} = 35$ W $\mathrm{cm^{-2}}$, and (c) $q''_{avg} = 62$ W $\mathrm{cm^{-2}}$. Numerical uncertainty range is shown in dotted light blue.

3.2.3. $G = 500\ kg\ m^{-2}\ s^{-1}$

Three cases were evaluated at G = 500 kg m^{-2} s^{-1} (Re $= 17{,}500 - 18{,}300$) with $q''_{avg} = 24 - 62$ W cm^{-2}. Simulation and correlation predictions for HTCs are summarized in Fig. 13 and Table 7. Simulation HTCs are found to increase slightly with heat flux, similar to the case with $G = 300$ kg m^{-2} s^{-1}. As in the cases with $G = 300$ kg m^{-2} s^{-1}, for this intermediate Re range, only the supercritical convection model of [76] shows close agreement with numerical predictions, and only for low-to-medium heat fluxes ($AAD = 3 - 34\%$). Similar to the G = 300 kg m^{-2} s^{-1} cases, the AAD values for all supercritical correlations increase with heat flux.

Table 7. Time-averaged LES simulation HTC values and correlations values for $G = 500$ kg m^{-2} s^{-1}

$q''_{avg}[W\ cm^{-2}]$ $q''_{bot}[W\ cm^{-2}]$ $q''_{sides}[W\ cm^{-2}]$ $q''_{top}[W\ cm^{-2}]$	$T_w\ [K]$	$Re\ [-]$	HTC_{sim} $[W\ m^{-2}K^{-1}]$	HTC_P [76] $[W\ m^{-2}K^{-1}]$ (AAD, LSD)	HTC_{JH} [77] $[W\ m^{-2}K^{-1}]$ (AAD, LSD)	HTC_{LZ} [75] $[W\ m^{-2}K^{-1}]$ (AAD, LSD)	HTC_{DB} [78] $[W\ m^{-2}K^{-1}]$ (AAD, LSD)
24 24 24 23	335.5	18,300	5,886	5,757 (3% , 0.01)	3,153 (87% , 0.27)	3,003 (96% , 0.29)	3,645 (61% , 0.21)
36 37 36 36	355.5	18,300	6,219	4,645 (34% , 0.13)	2,680 (132% , 0.37)	2,429 (156% , 0.41)	3,784 (64% , 0.22)
62 63 62 63	392.5	17,500	6,713	3,615 (86% , 0.27)	2,196 (206% , 0.49)	1,871 (259% , 0.55)	3,977 (69% , 0.23)

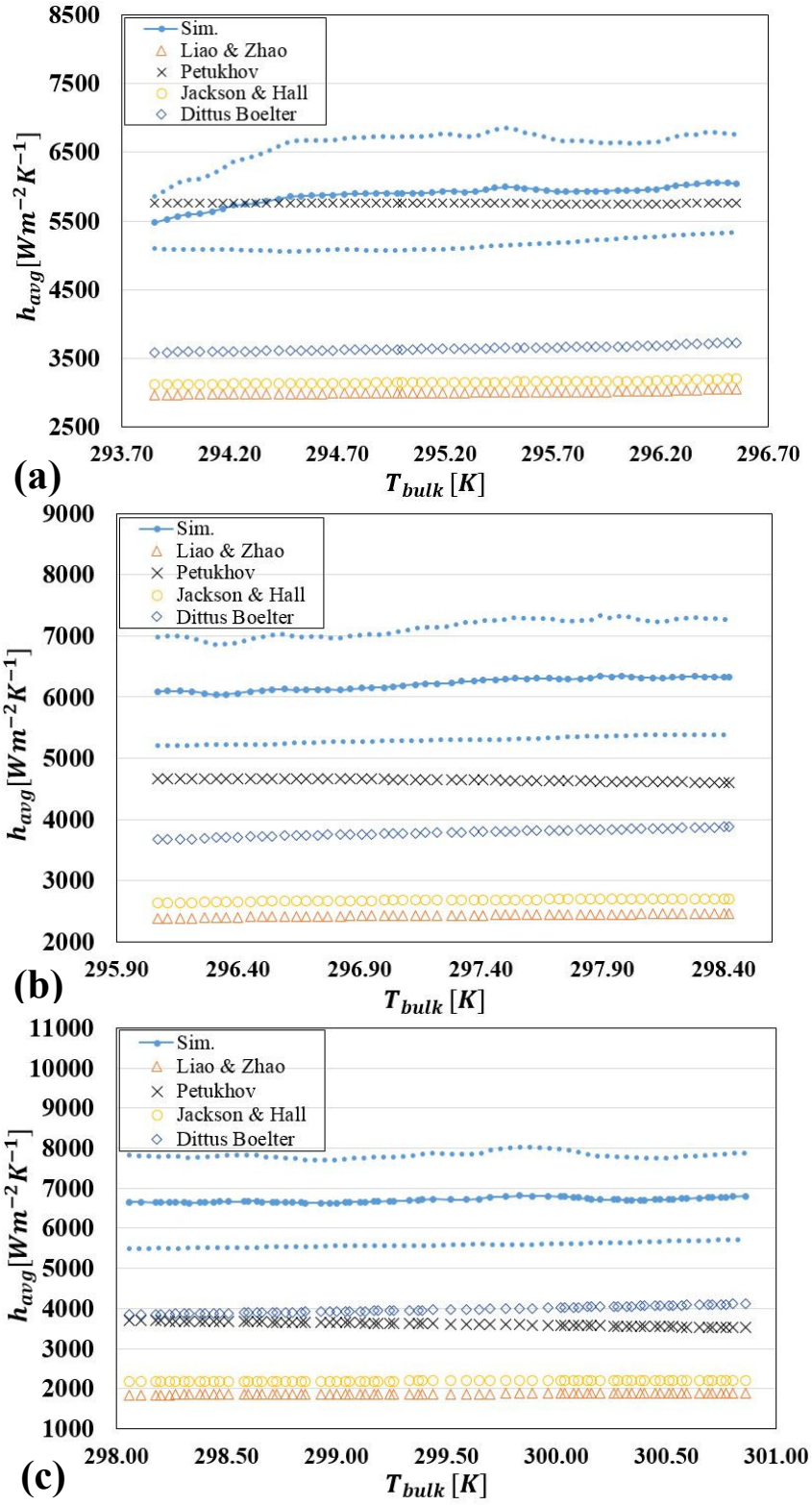

Figure 13. Average LES simulation and correlation HTC values vs. bulk fluid temperature for $G = 500$ kg $\mathrm{m^{-2}\ s^{-1}}$, and (a) $q''_{avg} = 24$ W $\mathrm{cm^{-2}}$, (b) $q''_{avg} = 36$ W $\mathrm{cm^{-2}}$, and (c) $q''_{avg} = 62$ W $\mathrm{cm^{-2}}$. The numerical uncertainty range is shown in dotted light blue.

3.2.4. $G = 1000\ kg\ m^{-2}\ s^{-1}$

Three cases were evaluated at the highest studied mass flux (G = 1000 kg m^{-2} s^{-1}, Re $= 34{,}200 - 35{,}700$) over a heat flux range of $q''_{avg} = 25 - 58$ W cm^{-2} (Fig. 14, Table 8). Close HTC agreement was found with the supercritical convection correlation of [76] ($AAD = 15 - 29\%$). AAD increased for all supercritical correlations with heat flux. Simulation HTCs decreased slightly with increasing heat flux, similar to the low Re – high heat flux cases ($G = 100$ kg m^{-2} s^{-1}).

Table 8. Time-averaged simulation and correlation predictions for HTCs for $G = 1000$ kg m^{-2} s^{-1}

$q''_{avg}[W\ cm^{-2}]$ $q''_{bot}[W\ cm^{-2}]$ $q''_{sides}[W\ cm^{-2}]$ $q''_{top}[W\ cm^{-2}]$	T_w [K]	Re [−]	HTC_{sim} $[W\ m^{-2}K^{-1}]$	HTC_P [76] $[W\ m^{-2}K^{-1}]$ (AAD, LSD)	HTC_{JH} [77] $[W\ m^{-2}K^{-1}]$ (AAD, LSD)	HTC_{LZ} [75] $[W\ m^{-2}K^{-1}]$ (AAD, LSD)	HTC_{DB} [78] $[W\ m^{-2}K^{-1}]$ (AAD, LSD)
25 25 25 24	319.7	34,200	9,030	12,753 (29% , 0.15)	6,582 (37% , 0.14)	5,085 (78% , 0.25)	6,064 (49% , 0.17)
33 32 34 32	329.7	35,700	8,962	10,704 (16% , 0.08)	5,760 (56% , 0.19)	4,208 (113% , 0.33)	6,100 (47% , 0.17)
58 58 58 59	359.7	35,700	8,936	7,773 (15% , 0.06)	4,430 (102% , 0.30)	2,969 (201% , 0.48)	6,200 (44% , 0.16)

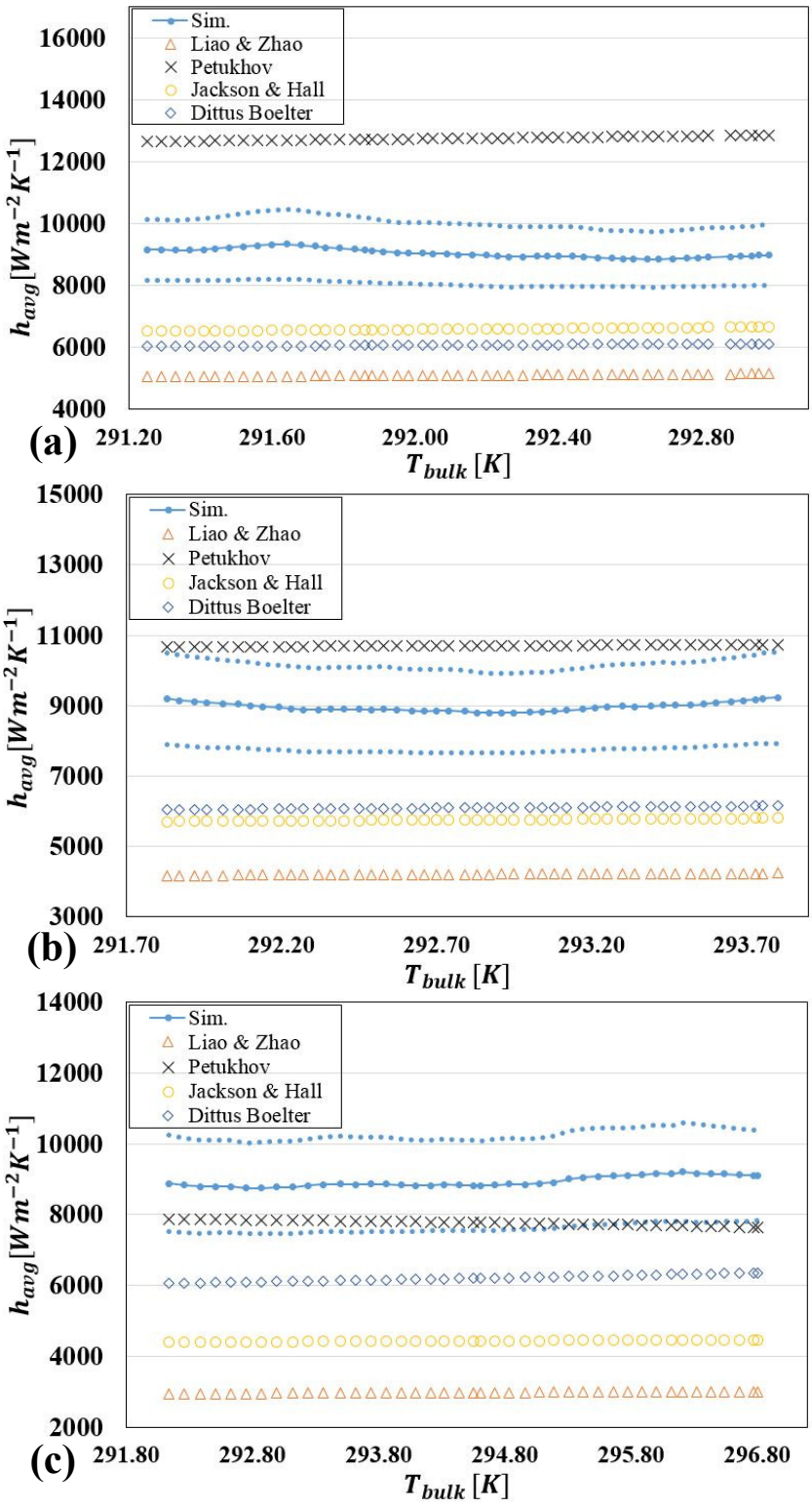

Figure 14. Average LES simulation and correlation HTC values vs. bulk fluid temperature for $G = 1000$ kg m^{-2} s^{-1}, and (a) $q''_{avg} = 25$ W cm^{-2}, (b) $q''_{avg} = 33$ W cm^{-2}, and (c) $q''_{avg} = 58$ W cm^{-2}. The numerical uncertainty range is shown in dotted light blue.

In the collaborative experimental effort by Jajja *et al.* [24], it was observed that for all cases, regardless of mass or heat flux, maximum HTC values were found when T_{bulk} approached T_{pc}. HTCs monotonically decreased with further increase in T_{bulk}. Similar trends were observed in our numerical study, where the studied temperature range covers T_{pc}, but only at higher range of heat flux (see Fig. 11 (b) and (c)). Jajja *et al.* [24] also reported that increasing average wall heat flux resulted in decreasing peak value of HTC. Our numerical findings also indicate that increasing wall heat flux results in decreasing average HTC for $G = 100\ \mathrm{kg\ m^{-2}\ s^{-1}}$ and $G = 1000\ \mathrm{kg\ m^{-2}\ s^{-1}}$.

3.3. Predicting Onset of Mixed Convection

The Richardson number (ratio of Grashof to Reynolds number squared) is often employed to define criteria for significant mixed convection effects [83].

$$\mathrm{Ri} = \frac{\mathrm{Gr}}{Re_{D_H}^2} = \left(\frac{g\beta(T_w - T_b)D_H^3}{\nu^2}\right)\Big/\left(\frac{\rho U D_H}{\mu}\right)^2 = \frac{g\beta(T_w - T_b)D_H}{U^2} \tag{7}$$

Here, β is the volumetric coefficient of thermal expansion, and μ and ν are the dynamic and kinematic viscosities, respectively. For nearly-constant-property channel flows, significant mixed convection is expected if Ri > 0.1 [84]. However, because thermophysical properties of supercritical fluids vary sharply and non-monotonically with temperature, defining a Ri threshold based on the fluid properties evaluated at the wall or bulk temperature may miss significant property variations within the thermal boundary layer itself. This is illustrated for a studied case in Fig. 15 ($G = 1000\ \mathrm{kg\ m^{-2}\ s^{-1}}$, $q''_{avg} = 33\ \mathrm{W\ cm^{-2}}$). If fluid properties are evaluated at the wall (T_w) or fluid bulk (T_b) temperatures, relatively low Ri values will be obtained. However, Ri values based on local temperatures may be ~10× greater. We therefore propose using the peak value of Ri in the thermal boundary layer ($\mathrm{Ri_{max}}$) as a metric for predicting the onset of mixed convection effects. To identify a critical value of $\mathrm{Ri_{max}}$ for mixed convection, $\mathrm{Ri_{max}}$ values and average heat fluxes on bottom and top walls are evaluated for each simulation case (Table 9).

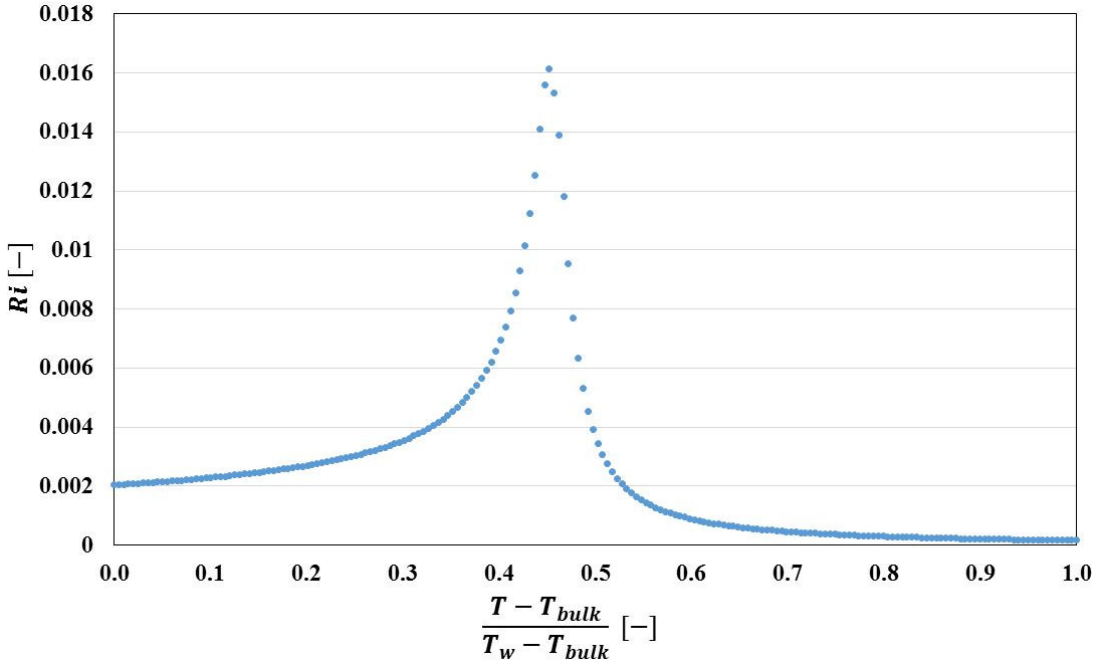

Figure 15. A representative curve of Ri as a function of temperature for the case of $G = 1000$ kg m^{-2} s^{-1}, and $q''_{avg} = 33$ W cm^{-2}

Here, we define the onset of significant mixed convection as when the bottom-to-top wall heat flux ratio $q''_{bot.avg}/q''_{top.avg}$ exceeds 1.1 (Fig. 16). Simulation data collapsed closely with a simple curve of $q''_{bot.avg}/q''_{top.avg}$ vs. Ri_{max}, suggesting consistent behavior between the studied cases. Based on these data, we propose a simple criterion for significant mixed convection of $\mathrm{Ri}_{max} > 0.5$.

To illustrate supercritical convection behavior without and with mixed convection, renderings of velocity and temperature fields are presented for two sample test cases with $G = 500$ kg m^{-2} s^{-1} (Ri_{max} = 0.07), and $G = 100$ kg m^{-2} s^{-1} (Ri_{max} = 5.0) (Figs. 17-18). For the case with mass flux of $G = 500$ kg m^{-2} s^{-1} with negligible mixed convection, velocity and thermal boundary layers appear almost symmetric on top and bottom walls (see Fig. 17). However, for the case with $G = 100$ kg m^{-2} s^{-1}, rising plumes are visible on the lower wall, and a thick stratified vapor-like layer is apparent near the upper wall (Fig. 18). This results in a bottom-to-top wall heat flux ratio of 2.10.

Table 9. Summary of the collected data for bottom wall to top wall heat flux ratio

$G\ [kg\ m^{-2}\ s^{-1}]$	$Re\ [-]$	$Ri_{max}\ [-]$	$q''_{bot.avg}$ $[W\ cm^{-2}]$	$q''_{top,avg}$ $[W\ cm^{-2}]$	$q''_{bot.avg}/q''_{top.avg}$ $[-]$
100	3,000	6.948	53.28	20.89	2.55
100	3,200	6.688	45.54	19.08	2.39
100	3,400	4.998	35.15	16.76	2.10
300	10,000	0.599	65.37	59.22	1.10
300	11,000	0.358	37.46	33.47	1.12
300	11,100	0.280	25.00	23.93	1.04
500	17,500	0.160	63.30	62.75	1.01
500	18,300	0.101	36.60	36.30	1.01
500	18,300	0.071	23.67	23.50	1.01
1,000	35,700	0.028	57.92	58.66	0.99
1,000	35,700	0.016	32.47	32.39	1.00
1,000	34,200	0.012	24.79	24.46	1.01

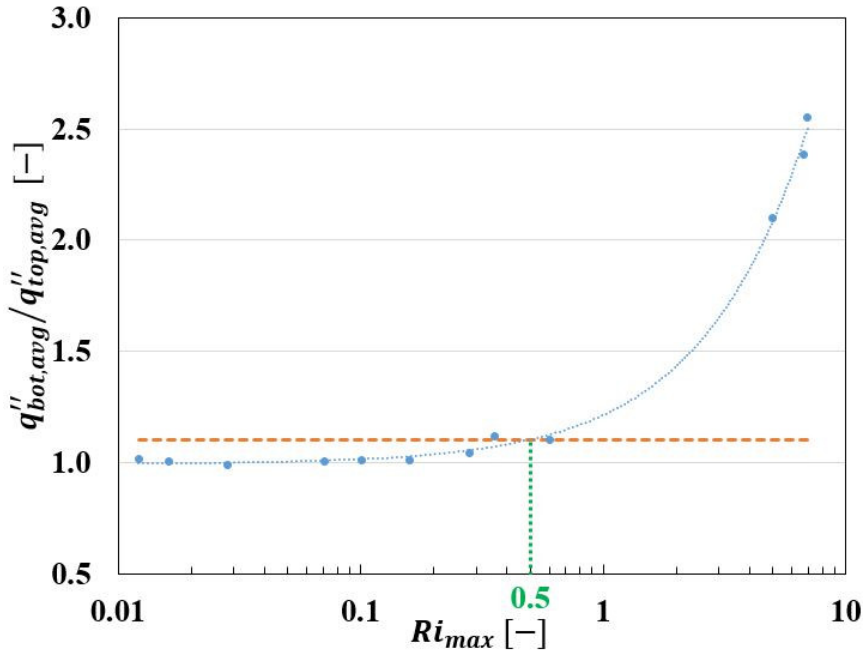

Figure 16. Bottom-to-top wall heat flux ratio vs. Ri_{max}, parabolic trendline fit in dashed line (R^2 = 0.998).

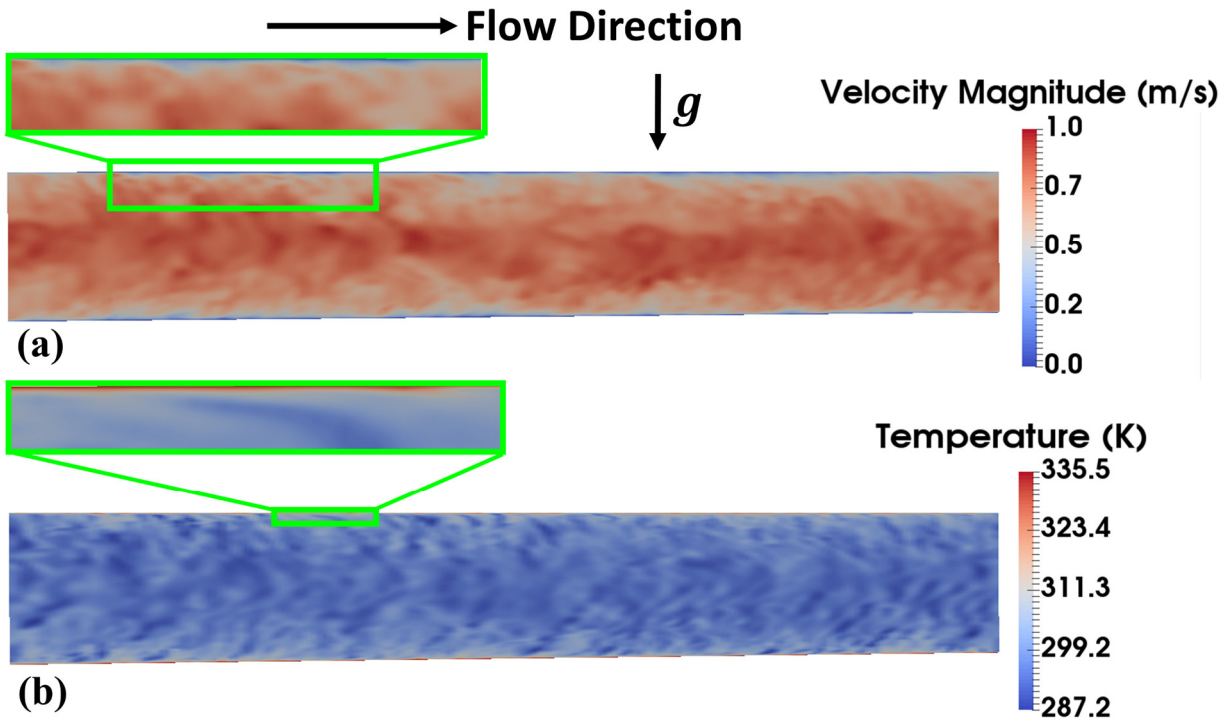

Figure 17. Simulation renderings for a case with $G = 500\ \text{kg m}^{-2}\ \text{s}^{-1}$ and $q'' = 24\ \text{W cm}^{-2}$ **a**. Cross-section velocity magnitude. **b**. Channel cross-section temperature field, with detail view of stratified flow near the top wall and thermal boundary layer (top 5% of channel).

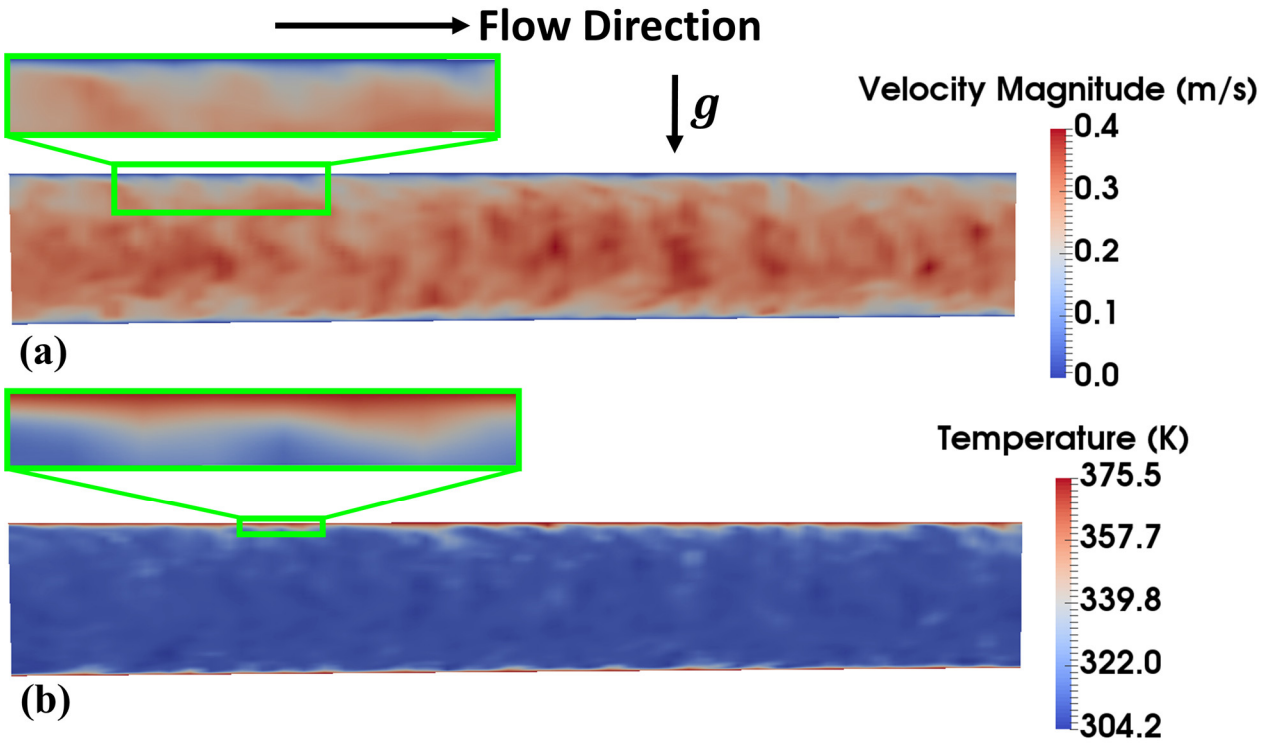

Figure 18. Simulation results for a case with $G = 100\ \text{kg m}^{-2}\ \text{s}^{-1}$ and $q'' = 27\ \text{W cm}^{-2}$ **a**. Cross-section velocity magnitude. **b**. Channel cross-section temperature field, with detail view of stratified flow near the top wall and thermal boundary layer (top 5% of channel).

3.4. Conjugate Heat Transfer Effects

In practical heat exchanger (HX) applications, local heat fluxes may vary because of mixed convection effects, as described in Section 3.3, and because of conjugate heat transfer effects (CHT) – coupling between fluid-domain convection and solid-domain conduction. Because local supercritical convection HTCs can vary sharply with wall temperatures, CHT effects may be more significant in supercritical HXs than typically encountered in sub-critical HXs.

To investigate the impact of CHT on supercritical HX performance, a representative microchannel heat sink is simulated, accounting for coupled conduction in stainless steel walls (thermal conductivity $k_S = 16.2\ \text{W m}^{-1}\ \text{K}^{-1}$). The solid domain is modeled as being thermally quasi-steady to reduce computational costs. The simulations were performed using a modified version of a conjugate heat transfer solver in OpenFOAM v1612+ [71] (chtMultiRegionFoam), which maintains a constant mass flux in a cyclic microchannel domain. Simulation results for the cooled device temperature, average channel wall temperature, and average HTC value are compared with analytic predictions using supercritical convection correlations [75–77] and the correlation of Dittus-Boelter [78].

The schematic of the studied geometry is shown in Fig. 19 and dimensions are listed in Table 10. The

microchannel is positioned at the center of solid domain, and the bottom of the solid block is heated with a constant Q_{tot} = 3 W (see Fig. 19). The side and top boundaries of the domain are modeled as adiabatic surfaces.

Simulation predictions are compared with those from an analytic thermal resistance network model (Fig. 20), incorporating the convection correlations. In this analysis, microchannel walls are modeled as finned structures, as suggested by [85,86]. In most microchannel heat exchangers, channel walls are relatively thick (low aspect ratio). Thus the 1-D fin analysis can only be considered as an approximation. For these cases, the fin analysis leads to 15 – 25% underestimation of $(T_w - T_{bulk})$ and $(T_{dev} - T_{bulk})$ compared with more accurate 2D conduction models. However, the simpler fin analysis is presented here as it is representative of typical practice in heat exchanger engineering.

$$R_{conv} = \frac{1}{\eta_o h A_{conv}} = \frac{1}{\eta_o h (W+H) L} \tag{8}$$

$$R_{cond} = \frac{L_{cond}}{k_S A_{cond}} = \frac{H_b}{k_S (0.5 \times W + t_{web}) L} \tag{9}$$

In Eqn. 8, η_o stands for overall finned surface efficiency. A system of equations (see Eqn. 10) was solved for each emprirical correlation [75–78] to predict device temperature T_{dev}, average wall temperature T_w, heat transfer coefficient h, fin efficiency η_f, and overall surface efficiency η_o, as a function of bulk fluid temperature T_{bulk} and Q_{tot}.

$$h = f(D_H, G, P, T_{bulk}, T_w)$$

$$Q_{tot} = h A_{conv} (T_w - T_{bulk})$$

$$\eta_f = \frac{\tanh(mL)}{mL}, m = \sqrt{\frac{h \times per_{fin}}{k_S A_c}}$$

$$\eta_o = 1 - \frac{A_{s,fin}}{A_{tot}} (1 - \eta_f)$$

$$Q_{tot} = \frac{T_{dev} - T_{bulk}}{R_{cond} + R_{conv}} \tag{10}$$

In Eqn. 10, fin perimeter $per_{fin} = L$, fin cross-sectional area $A_c = t_{web} L$, fin surface area $A_{s,fin} = (0.5 \times W + H)L$, and total surface area $A_{tot} = A_{s,b} - A_c + A_{s,fin}$, where base surface area $A_{s,b} = (0.5 \times W + t_{web})$.

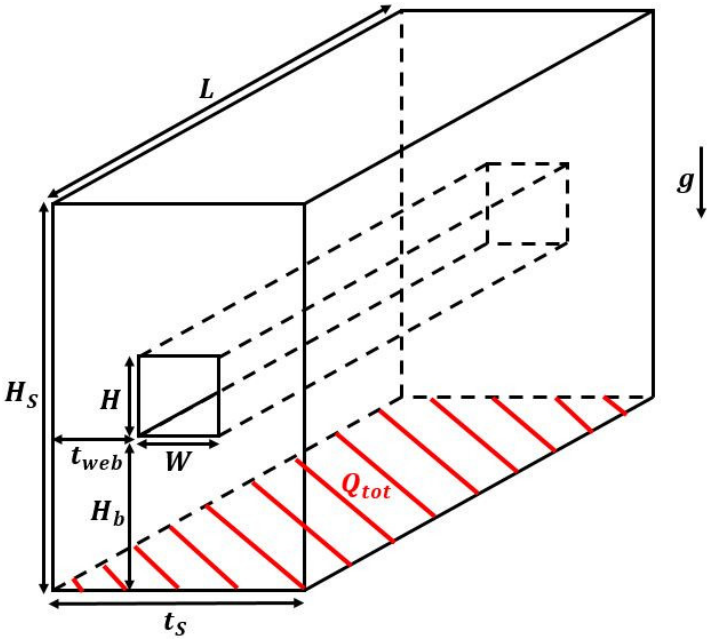

Figure 19. Schematic of the CHT case simulation geometry

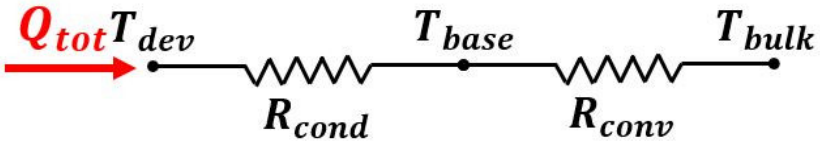

Figure 20. Schematic of CHT study heat resistance network

Table 10. Dimensions of the computational CHT domain

Section	Size
Channel Width (W)	750.02 µm
Channel Height (H)	737.32 µm
Channel Length (L)	5 mm
Solid Domain Height (H_S)	4 mm
Channel Base Height (H_b)	1.63 mm
Solid Domain Thickness (t_S)	1.74 mm
Web Thickness (t_{web})	495.93 µm

A high heat flux-low mass flux case of $G = 100\ \text{kg m}^{-2}\ \text{s}^{-1}$ and input heating power of $Q_{tot} = 3\ W$ was selected to represent a case for which large deviations in heat transfer performance may be expected between simulations and analytic models incorporating convection correlations ([75–78]). Plots of simulation average HTCs, average predicted wall temperature T_w, and predicted device temperature T_{dev} (at the bottom side of solid domain where Q_{tot} is applied) vs. bulk flow temperature are shown and compared with the analytic models in Fig. 21 and Table 11. The simulation uncertainty range for T_w and T_{dev} was less than 2%, and therefore not apparent in Fig. 21. The trend of predicted HTC continuously decreasing with increasing T_{bulk} agrees with the analytic model using the correlation of Petukhov *et al.* [76]. The other three correlations, *i.e.* Liao and Zhao [75], Jackson and Hall [77], and Dittus-Boelter [78], yield a maximum HTC value around T_{pc} (Fig. 21(a)). Overall, there is a large (7×) deviation between correlation HTC values. The models of [75,77,78] predict that minimum T_w and T_{dev} occur for $T_{\text{bulk}} \sim T_{\text{pc}}$ (Fig. 21b-c). Overall, the T_w and T_{dev} values predicted using the three supercritical correlations [75–77] and analytic model deviate widely and vary sharply with T_{bulk}. Only a minor portion of the errors can be attributed the 1-D conduction fin approximation rather than the heat transfer correlations. The analytic model result using the Dittus-Boelter [78] correlation yields the closest agreement with the simulation results for $T_{bulk} < 305\ K\ \left(AAD_{T_w} < 10\%, and\ AAD_{T_{dev}} < 20\%\right)$. However, at higher bulk fluid temperatures ($T_{bulk} \sim T_{pc}$) the correlations of Liao and Zhao [75] and Petukhov *et al.* [76] show closest agreement with the simulation T_{pc} ($AAD < 20\%\ for\ both\ T_w$ and T_{dev}).

This CHT study highlights the limitations of currently available analytic models for supercritical convection, and the need for further research in high-heat-flux microchannel flows. A heat exchanger designed using these correlations could yield errors in driving temperature differences by ~3× (Fig. 21c), leading to catastrophic hardware failure.

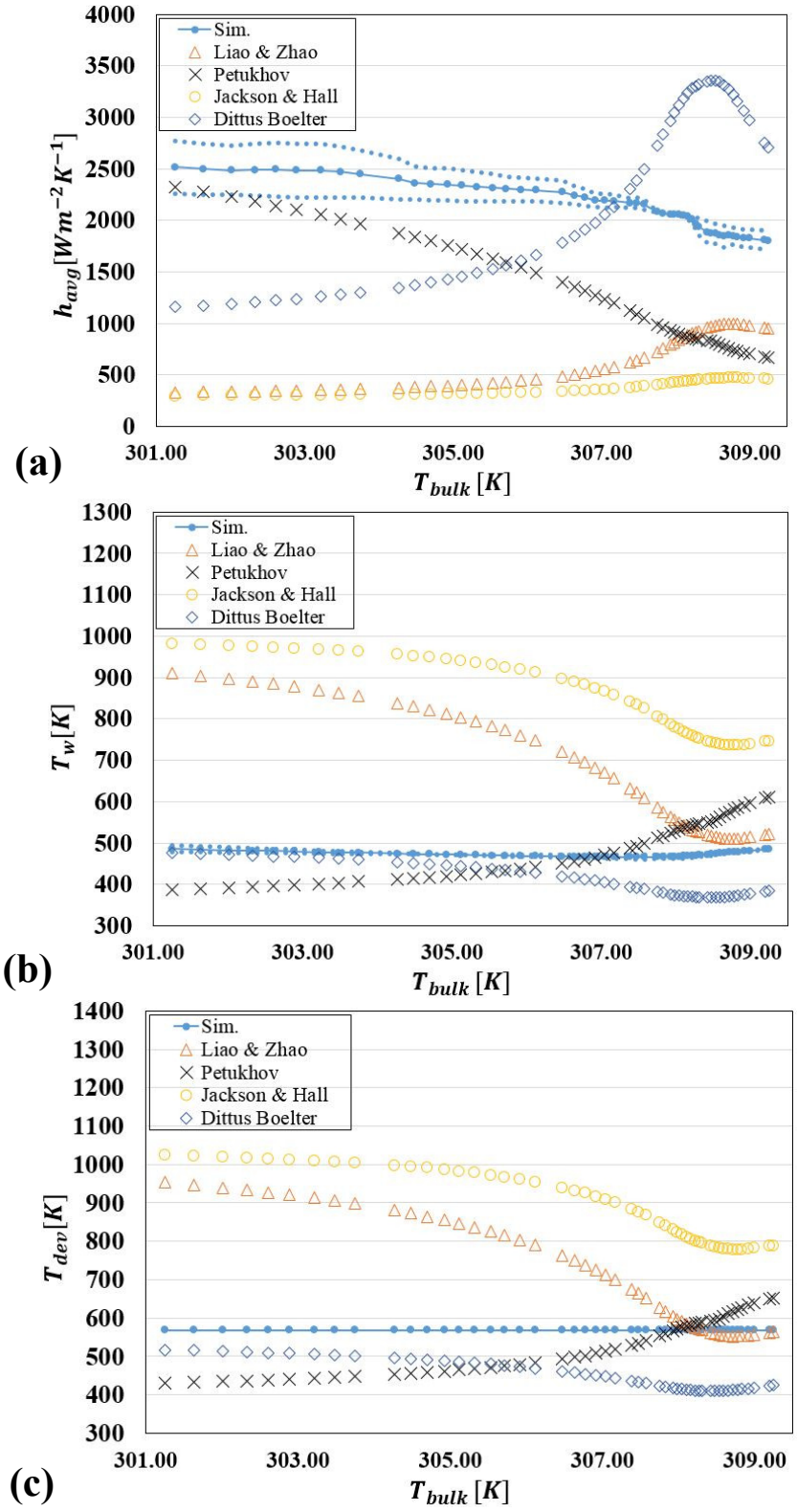

Figure 21. Average LES simulation and analytic model predictions ($G = 100$ kg $\mathrm{m}^{-2}\,\mathrm{s}^{-1}$ and $Q_{tot} = 3\,W$) for (a) HTC values , (b) average predicted wall temperature T_w, and (c) predicted device temperature T_{dev}. The numerical uncertainty range is shown in dotted light blue.

Table 11. Average LES simulation HTCs and predictions with correlations in CHT study ($G = 100$ kg m^{-2} s^{-1})

$q''_{avg}[W\ cm^{-2}]$ $q''_{bot}[W\ cm^{-2}]$ $q''_{sides}[W\ cm^{-2}]$ $q''_{top}[W\ cm^{-2}]$	$T_{w,avg}[K]$ $T_{bot}[K]$ $T_{sides}[K]$ $T_{top}[K]$	Re [−]	HTC_{sim} $[W\ m^{-2}K^{-1}]$	HTC_P [76] $[W\ m^{-2}K^{-1}]$ (AAD, LSD)	HTC_{JH} [77] $[W\ m^{-2}K^{-1}]$ (AAD, LSD)	HTC_{LZ} [75] $[W\ m^{-2}K^{-1}]$ (AAD, LSD)	HTC_{DB} [78] $[W\ m^{-2}K^{-1}]$ (AAD, LSD)
41	473.1	3,000	2,160	1,305 (86%, 0.22)	382 (493%, 0.75)	651 (307%, 0.52)	2,273 (49%, 0.02)
62	486.7						
40	471.4						
22	462.8						

4. Conclusions

This study presented a computational LES investigation of supercritical CO_2 microchannel convection phenomena with non-uniform heat fluxes. A mesh convergence and numerical uncertainty study was first conducted for the simulation approach. The simulation approach was validated using experimental data [24].

Twelve cases were evaluated for reduced pressure $P_r = 1.1$, mass flux $G = 100 - 1{,}000$ kg m^{-2} s^{-1} ($Re = 3{,}000 - 35{,}700$), and wall heat flux $q'' = 24 - 62$ W cm^{-2}. Convection heat transfer coefficients were compared with available supercritical correlations (Petukhov *et al.* [76]; Jackson and Hall [77]; and Liao and Zhao [75]) and the constant-property correlation of Dittus-Boelter [78]. Results were used to assess the validity of these correlations for supercritical microchannel convection. The bottom-to-top wall HTC ratios from these simulation cases were adopted to identify a new criterion for the onset of mixed convection in microscale supercritical fluid flows. Finally, a CHT case was studied to explore the effects of coupled solid- and fluid-phase transport, as encountered in actual heat exchangers.

The main findings of this study for near-critical-point microchannel sCO_2 convection include:

1. As heat flux increases, HTCs at the microchannel walls decrease for low and high mass fluxes ($G = 100$ kg m^{-2} s^{-1} *and* $G = 1000$ kg m^{-2} s^{-1}). However, HTCs increase for intermediate mass flux values ($G = 300$ kg m^{-2} s^{-1} *and* $G = 500$ kg m^{-2} s^{-1}).
2. At the highest studied range of heat flux ($q'' = 58 - 62$ W cm^{-2}), all assessed supercritical correlations were found to significantly under-predict HTCs. In an earlier investigation [4], the concept of supercritical-fluid based high-heat-flux electronics thermal management solutions was explored. However, the wide discrepancies between supercritical convection correlations and relatively low HTCs predicted with such correlations made the feasibility of such thermal management devices unclear. The present findings of

heat transfer coefficients of 2-4× greater than those predicted with earlier correlations suggests the great potential of supercritical-fluid-based thermal management solutions for high-power devices.

3. Of the three available supercritical correlations, only the model of Petukhov *et al.* [76] shows consistent agreement with the simulation results for wall temperatures $T_w < 360\ K$.
4. At low mass fluxes ($G = 100\ \mathrm{kg\ m^{-2}\ s^{-1}}$), non-uniform HTCs (with a maximum deviation of 155%) were observed at different walls due to mixed-convection induced stratification. This non-uniform heating effect on different microchannel walls has not been quantified in prior supercritical convection models.
5. Due to sharp properties variations with temperature, mixed convection effects cannot be reliably predicted using parameters (*e.g.*, Ri) evaluated at either wall or bulk flow temperatures. Instead, we recommend using a maximum Richardson number ($\mathrm{Ri_{max}}$), which is the greatest value of Ri obtained using property values evaluated over the range of T_w to T_b. Significant mixed convection effects (>10% difference in HTC between top and bottom walls) occur for $\mathrm{Ri_{max}} > 0.5$.
6. Based on the CHT study, it was found that empirical supercritical correlations can lead to dramatic variations in predicted HTC, wall temperature, and heat source temperature values in typical heat exchanger geometries. HTC values can vary over 7× between models. Thus, great care must be taken when designing heat exchangers for low mass flux operation at near-critical point conditions.

The current LES-based simulation approach can be applied to investigate micro-scale convection for other working pressures and supercritical fluids. Currently, minimal data are available for supercritical convection with fluids other than water and CO_2. Investigations for other channel orientations (vertical upward/downward, inclined) are also needed. Investigations into supercritical convection in enhanced heat transfer geometries, such as ribbed passages and pin-fin arrays are needed to inform emerging heat exchanger designs.

Acknowledgements

The authors wish to acknowledge generous support from the U.S. National Science Foundation (CBET-1604538), and computing resources from Penn State ACI and NSF XSEDE (award number CTS170047).

References

[1] Lin, S., Sefiane, K., and Christy, J. R. E., 2002, "Prospects of Confined Flow Boiling in Thermal Management of Microsystems," Appl. Therm. Eng., **22**(7), pp. 825–837.

[2] Kandlikar, S. G., and Grande, W. J., 2004, "Evaluation of Single Phase Flow in Microchannels for High Heat Flux Chip Cooling—Thermohydraulic Performance Enhancement and Fabrication Technology," Heat Transf. Eng., **25**(8), pp. 5–16.

[3] Zada, K. R., Drost, M. K., and Fronk, B. M., 2015, "Application of Microscale Devices for Megawatt Scale Concentrating Solar Power Plants," *2015 ASME International Mechanical Engineering Congress and Exposition*, Houston, TX.

[4] Fronk, B. M., and Rattner, A. S., 2016, "High-Flux Thermal Management With Supercritical Fluids," J. Heat Transfer, **138**(12), article 124501.

[5] Iverson, B. D., Conboy, T. M., Pasch, J. J., and Kruizenga, A. M., 2013, "Supercritical CO2 Brayton Cycles for Solar-Thermal Energy," Appl. Energy, **111**, pp. 957–970.

[6] Dieter, C. A., Linsey, K. S., Caldwell, R. R., Harris, M. A., Ivahnenko, T. I., Lovelace, J. K., Maupin, M. A., and Barber, N. L., 2017, "Estimated Use of Water in the United States County-Level Data for 2015: US Geological Survey Data Release."

[7] Turchi, C. S., Ma, Z., Neises, T. W., and Wagner, M. J., 2013, "Thermodynamic Study of Advanced Supercritical Carbon Dioxide Power Cycles for Concentrating Solar Power Systems," J. Sol. Energy Eng., **135**(4), article 041007.

[8] National Renewable Energy Laboratory, 2003, *Assessment of Parabolic Trough and Power Tower Solar Technology Cost and Performance Forecasts. Report NREL/SR-550-34440*, Chicago, IL.

[9] Kolb, G., Ho, C., Mancini, T., and Gary, J., 2011, "Power Tower Technology Roadmap and Cost Reduction Plan," *Report* SAND2011-2419, Sandia National Laboratories, Albuquerque, NM.

[10] Pioro, I., and Mokry, S., 2011, "Heat Transfer to Supercritical Fluids," *Heat Transfer-Theoretical Analysis, Experimental Investigations and Industrial Systems*, InTech.

[11] Ackerman, J. W., 1970, "Pseudoboiling Heat Transfer to Supercritical Pressure Water in Smooth and Ribbed Tubes," J. Heat Transfer, **92**(3), pp. 490-497.

[12] Wang, J., Li, H., Yu, S., and Chen, T., 2011, "Investigation on the Characteristics and Mechanisms of Unusual Heat Transfer of Supercritical Pressure Water in Vertically-Upward Tubes," Int. J. Heat Mass Transf., **54**(9–10), pp. 1950–1958.

[13] Pioro, I. L., and Duffey, R. B., 2007, *Heat-Transfer Enhancement at Supercritical Pressures*, ASME Press.

[14] Bringer, R. P., and Smith, J. M., 1957, "Heat Transfer in the Critical Region," AIChE J., **3**(1), pp. 49–55.

[15] Dittus, F.W., Boelter, L. M. K., 1930, *Heat Transfer in Automobile Radiators of the Tubular Type*, Report, University of California, Berkeley.

[16] Krasnoshchekov, E. A., and Protopopov, V. S., 1966, "Experimental Study of Heat Exchange in Carbon Dioxide in the Supercritical Range at High Temperature Drops," High Temp., **4**, pp. 375–382.

[17] Wood, R. D., and Smith, J. M., 1964, "Heat Transfer in the Critical Region—temperature and Velocity Profiles in Turbulent Flow," AIChE J., **10**(2), pp. 180–186.

[18] Tanaka, H., Nishiwaki, N., and Hirata, M., 1967, "Turbulent Heat Transfer to Supercritical Carbon Dioxide," *JSME Semi-International Symposium*, JSME, Tokyo, Japan, pp. 127–134.

[19] Shiralkar, B., and Griffith, P., 1970, "The Effect of Swirl, Inlet Conditions, Flow Direction, and Tube Diameter on the Heat Transfer to Fluids at Supercritical Pressure," J. Heat Transfer, **92**(3), p. 465.

[20] Swenson, H. S., Carver, J. R., and Kakarala, C. R., 1965, "Heat Transfer to Supercritical Water in Smooth-Bore Tubes," J. Heat Transfer, **87**(4), pp. 477–484.

[21] Yamagata, K., Nishikawa, K., Hasegawa, S., Fujii, T., and Yoshida, S., 1972, "Forced Convective Heat Transfer to Supercritical Water Flowing in Tubes," Int. J. Heat Mass Transf., **15**(12), pp. 2575–2593.

[22] Kirillov, P. L., Yur'ev, Y. S., and Bobkov, V. P., 1990, *Handbook of Thermal-Hydraulics Calculations (in Russian)*, Energoatomizdat Publishing House, Moscow, Russia.

[23] Jackson, J. D., 2002, "Consideration of the Heat Transfer Properties of Supercritical Water in Connection with the Cooling of Advanced Nuclear Reactors," *13th Pacific Basin Nuclear Conference*, Shenzhen City, China.

[24] Jajja, S. A., Zada, K. R., and Fronk, B. M., 2019, "Experimental Investigation of Supercritical Carbon Dioxide in Horizontal Microchannels with Non-Uniform Heat Flux Boundary Conditions," Int. J. Heat Mass Transf., **130**, pp. 304–319.

[25] Liao, S. M., and Zhao, T. S., 2002, "Measurements of Heat Transfer Coefficients From Supercritical Carbon Dioxide Flowing in Horizontal Mini/Micro Channels," J. Heat Transfer, **124**(3), p. 413.

[26] Pitla, S., Robinson, D., Groll, E., and Ramadhyani, S., 1998, "Heat Transfer from Supercritical Carbon Dioxide in Tube Flow: A Critical Review," HVAC&R Res., **4**(3), pp. 281–301.

[27] Pitla, S. S., Groll, E. A., and Ramadhyani, S., 2002, "New Correlation to Predict the Heat Transfer Coefficient during In-Tube Cooling of Turbulent Supercritical CO2," Int. J. Refrig., **25**(7), pp. 887–895.

[28] Dang, C., and Hihara, E., 2004, "In-Tube Cooling Heat Transfer of Supercritical Carbon Dioxide. Part 1. Experimental Measurement," Int. J. Refrig., **27**(7), pp. 736–747.

[29] Yoon, S. H., Kim, J. H., Hwang, Y. W., Kim, M. S., Min, K., and Kim, Y., 2003, "Heat Transfer and Pressure Drop Characteristics during the In-Tube Cooling Process of Carbon Dioxide in the Supercritical Region," Int. J. Refrig., **26**(8), pp. 857–864.

[30] Groll, E. A., and Kim, J.-H., 2007, "Review of Recent Advances toward Transcritical CO2 Cycle Technology," HVAC&R Res., **13**(3), pp. 499–520.

[31] Fronk, B. M., and Garimella, S., 2011, "Water-Coupled Carbon Dioxide Microchannel Gas Cooler for Heat Pump Water Heaters: Part I - Experiments," Int. J. Refrig., **34**(1), pp. 7–16.

[32] Fronk, B. M., and Garimella, S., 2011, "Water-Coupled Carbon Dioxide Microchannel Gas Cooler for Heat Pump Water Heaters: Part II – Model Development and Validation," Int. J. Refrig., **34**(1), pp. 17–28.

[33] Kim, M.-H., Pettersen, J., and Bullard, C. W., 2004, "Fundamental Process and System Design Issues in CO2 Vapor Compression Systems," Prog. Energy Combust. Sci., **30**(2), pp. 119–174.

[34] Deissler, R. G., 1954, "Heat Transfer and Fluid Friction for Fully Developed Turbulent Flow of Air and Supercritical Water with Variable Fluid Properties," Trans. ASME, **76**(1), pp. 73–85.

[35] Koppel, L. B., and Smith, J. M., 1961, "Turbulent Heat Transfer in the Critical Region," Int. Dev. Heat Transf., pp. 585–590.

[36] Adebiyi, G. A., and Hall, W. B., 1976, "Experimental Investigation of Heat Transfer to Supercritical Pressure Carbon Dioxide in a Horizontal Pipe," Int. J. Heat Mass Transf., **19**(7), pp. 715–720.

[37] Schnurr, N. M., Sastry, V. S., and Shapiro, A. B., 1976, "A Numerical Analysis of Heat Transfer to Fluids Near the Thermodynamic Critical Point Including the Thermal Entrance Region," J. Heat Transfer, **98**(4), p. 609.

[38] Bellmore, C. P., and Reid, R. L., 1983, "Numerical Prediction of Wall Temperatures for Near-Critical Para-Hydrogen in Turbulent Upflow Inside Vertical Tubes," J. Heat Transfer, **105**(3), pp. 536-541.

[39] Bellinghausen, R., and Renz, U., 1990, "Pseudocritical Heat Transfer inside Vertical Tubes," Chem. Eng. Process. Process Intensif., **28**(3), pp. 183–186.

[40] Koshizuka, S., Takano, N., and Oka, Y., 1995, "Numerical Analysis of Deterioration Phenomena in Heat Transfer to Supercritical Water," Int. J. Heat Mass Transf., **38**(16), pp. 3077–3084.

[41] Menter, F. R., 1992, "Improved Two-Equation k-Omega Turbulence Models for Aerodynamic Flows," NASA STI/Recon Tech. Rep. Number 103975.

[42] Dang, C., and Hihara, E., 2004, "In-Tube Cooling Heat Transfer of Supercritical Carbon Dioxide. Part 2. Comparison of Numerical Calculation with Different Turbulence Models," Int. J. Refrig., **27**(7), pp. 748–760.

[43] He, S., Jiang, P.-X., Xu, Y.-J., Shi, R.-F., Kim, W. S., and Jackson, J. D., 2005, "A Computational Study of Convection Heat Transfer to CO2 at Supercritical Pressures in a Vertical Mini Tube," Int. J. Therm. Sci., **44**(6), pp. 521–530.

[44] Asinari, P., 2005, "Numerical Prediction of Turbulent Convective Heat Transfer in Mini/Micro Channels for Carbon Dioxide at Supercritical Pressure," Int. J. Heat Mass Transf., **48**(18), pp. 3864–3879.

[45] Cheng, X., Kuang, B., and Yang, Y., 2007, "Numerical Analysis of Heat Transfer in Supercritical Water Cooled Flow Channels," Nucl. Eng. Des., 237(3), pp. 240-252.

[46] Yang, J., Oka, Y., Ishiwatari, Y., Liu, J., and Yoo, J., 2007, "Numerical Investigation of Heat Transfer in Upward Flows of Supercritical Water in Circular Tubes and Tight Fuel Rod Bundles," Nucl. Eng. Des., **237**(4), pp. 420–430.

[47] Sharabi, M., Ambrosini, W., and He, S., 2008, "Prediction of Unstable Behaviour in a Heated Channel

with Water at Supercritical Pressure by CFD Models," Ann. Nucl. Energy., 35(5), pp. 767-782.

[48] He, S., Kim, W. S., and Bae, J. H., 2008, "Assessment of Performance of Turbulence Models in Predicting Supercritical Pressure Heat Transfer in a Vertical Tube," Int. J. Heat Mass Transf., **51**(19–20), pp. 4659–4675.

[49] Wen, Q. L., and Gu, H. Y., 2010, "Numerical Simulation of Heat Transfer Deterioration Phenomenon in Supercritical Water through Vertical Tube," Ann. Nucl. Energy, **37**(10), pp. 1272–1280.

[50] Du, Z., Lin, W., and Gu, A., 2010, "Numerical Investigation of Cooling Heat Transfer to Supercritical CO2 in a Horizontal Circular Tube," J. Supercrit. Fluids, **55**(1), pp. 116–121.

[51] Zhang, B., Shan, J., and Jiang, J., 2010, "Numerical Analysis of Supercritical Water Heat Transfer in Horizontal Circular Tube," Prog. Nucl. Energy, **52**(7), pp. 678–684.

[52] Mohseni, M., and Bazargan, M., 2011, "The Effect of the Low Reynolds Number K-e Turbulence Models on Simulation of the Enhanced and Deteriorated Convective Heat Transfer to the Supercritical Fluid Flows," Heat Mass Transf., **47**(5), pp. 609–619.

[53] Liu, L., Xiao, Z., Yan, X., Zeng, X., and Huang, Y., 2013, "Numerical Simulation of Heat Transfer Deterioration Phenomenon to Supercritical Water in Annular Channel," Ann. Nucl. Energy, **53**, pp. 170–181.

[54] Pucciarelli, A., Borroni, I., Sharabi, M., and Ambrosini, W., 2015, "Results of 4-Equation Turbulence Models in the Prediction of Heat Transfer to Supercritical Pressure Fluids," Nucl. Eng. Des., **281**, pp. 5–14.

[55] Zhu, X., Morooka, S., and Oka, Y., 2014, "Numerical Investigation of Grid Spacer Effect on Heat Transfer of Supercritical Water Flows in a Tight Rod Bundle," Int. J. Therm. Sci., **76**, pp. 245–257.

[56] Grunloh, T. P., 2019, "Four Equation K-Omega Based Turbulence Model with Algebraic Flux for Supercritical Flows," Ann. Nucl. Energy, **123**, pp. 210–221.

[57] Bae, J. H., Yoo, J. Y., and Choi, H., 2005, "Direct Numerical Simulation of Turbulent Supercritical Flows with Heat Transfer," Phys. Fluids, **17**(10).

[58] Bae, J. H., Yoo, J. Y., and McEligot, D. M., 2008, "Direct Numerical Simulation of Heated CO2 Flows at Supercritical Pressure in a Vertical Annulus at Re= 8900," Phys. Fluids, **20**(5), Article 55108.

[59] Yoo, J. Y., 2013, "The Turbulent Flows of Supercritical Fluids with Heat Transfer," Annu. Rev. Fluid Mech., **45**(1), pp. 495–525.

[60] Azih, C., Brinkerhoff, J. R., and Yaras, M. I., 2012, "Direct Numerical Simulation of Convective Heat Transfer in a Zero-Pressure-Gradient Boundary Layer with Supercritical Water," J. Therm. Sci., **21**(1), pp. 49–59.

[61] Licht, J., Anderson, M., and Corradini, M., 2009, "Heat Transfer and Fluid Flow Characteristics in Supercritical Pressure Water," J. Heat Transfer, **131**(7), Article 072502.

[62] Chu, X., and Laurien, E., 2016, "Flow Stratification of Supercritical CO2 in a Heated Horizontal Pipe," J.

Supercrit. Fluids, **116**, pp. 172–189.

[63] Pandey, S., Chu, X., Laurien, E., and Weigand, B., 2018, "Buoyancy Induced Turbulence Modulation in Pipe Flow at Supercritical Pressure under Cooling Conditions," Phys. Fluids, **30**(6).

[64] Ničeno, B., and Sharabi, M., 2013, "Large Eddy Simulation of Turbulent Heat Transfer at Supercritical Pressures," Nucl. Eng. Des., **261**, pp. 44-55.

[65] Nabil, M., and Rattner, A. S., 2018, "LES Simulation of Turbulent Supercritical CO2 Heat Transfer in Microchannels," *Proceedings of the 6th International Supercritical CO2 Power Cycles Symposium*, Pittsburgh, PA.

[66] Nabil, M., and Rattner, A. S., 2018, "Heat Transfer Performance of Heated Upward Turbulent Supercritical CO2 Flow in a Microchannel: A Numerical Study," *Proceedings of the 6th International Conference on Micro and Nano Flows (MNF2018)*, Atlanta, GA.

[67] Ducros, F., Nicoud, F., and Poinsot, T., 1998, "Wall-Adapting Local Eddy-Viscosity Models for Simulations in Complex Geometries," Numer. Methods Fluid Dyn. VI, pp. 293–299.

[68] Peng, D.-Y., and Robinson, D. B., 1976, "A New Two-Constant Equation of State," Ind. Eng. Chem. Fundam., **15**(1), pp. 59–64.

[69] Fenghour, A., Wakeham, W. A., and Vesovic, V., 1998, "The Viscosity of Carbon Dioxide," J. Phys. Chem. Ref. Data, **27**(1), pp. 31–44.

[70] Vesovic, V., Wakeham, W. A., Olchowy, G. A., Sengers, J. V., Watson, J. T. R., and Millat, J., 1990, "The Transport Properties of Carbon Dioxide," J. Phys. Chem. Ref. Data, **19**(3), p. 763.

[71] OpenCFD Ltd., 2016, "OpenFOAM V1612+."

[72] Kays, W. M., 2005, *Convective Heat and Mass Transfer*, McGraw-Hill Publications, pp. 312-317.

[73] Moin, P., and Kim, J., 1985, "Numerical Investigation of Turbulent Channel Flow," J. Fluid Mech., **118**, pp. 341–377.

[74] Dong, Y. H., Lu, X. Y., and Zhuang, L. X., 2002, "An Investigation of the Prandtl Number Effect on Turbulent Heat Transfer in Channel Flows by Large Eddy Simulation," Acta Mech., **159**, pp. 39–51.

[75] Liao, S. M., and Zhao, T. S., 2002, "An Experimental Investigation of Convection Heat Transfer to Supercritical Carbon Dioxide in Miniature Tubes," Int. J. Heat Mass Transf., **45**(25), pp. 5025–5034.

[76] Petukhov, B. S., Krasnoschekov, E. A., and Protopopov, V. S., 1961, "An Investigation of Heat Transfer to Fluids Flowing in Pipes under Supercritical Conditions," *1961 International Heat Transfer Conference*, ASME, Boulder, CO, pp. 569–578.

[77] Jackson, J. D., and Hall, W. B., 1979, "Forced Convection Heat Transfer to Fluids at Supercritical Pressure," *Turbulent Forced Convection in Channels and Bundles: Theory and Applications to Heat Exchangers and Nuclear Reactors*, B. Spalding, and S. Kakac, eds., Hemisphere Publishing Corporation, pp. 563–611.

[78] Dittus, F. W., and Boelter, L. M. K., 1985, "Heat Transfer in Automobile Radiators of the Tubular Type,"

Int. Commun. Heat Mass Transf., **12**(1), pp. 3–22.

[79] Celik, I. B., Ghia, U., Roache, P. J., Freitas, C. J., Coleman, H., and Raad, P. E., 2008, "Procedure for Estimation and Reporting of Uncertainty Due to Discretization in CFD Applications," J. Fluids Eng., **130**(7), Article 78001.

[80] Gnielinski, V., 1976, "New Equations for Heat and Mass Transfer in Turbulent Pipe and Channel Flow," Int. Chem. Eng., **16**(2), pp. 359–368.

[81] COMSOL Inc., 2017, "COMSOL, v. 5.3."

[82] Bishop, A. A., Sandberg, R. O., and Tong, L. S., 1964, *Forced-Convection Heat Transfer to Water at near-Critical Temperatures and Supercritical Pressures*, Westinghouse Electric Corp., Pittsburgh, Pa. Atomic Power Div.

[83] Gebhart, B., Jaluria, Y., Mahajan, R. L., Sammakia, B., 1988, *Buoyancy-Induced Flows and Transport*, Hemisphere Publishing Corporation, New York.

[84] Turner, J. S., 1979, *Buoyancy Effects in Fluids*, Cambridge University Press.

[85] Nagavarapu, A. K., and Garimella, S., 2011, "Design of Microscale Heat and Mass Exchangers for Absorption Space Conditioning Applications," J. Therm. Sci. Eng. Appl., **3**(2), Article 021005.

[86] Delahanty, J. C., 2015, "Desorption of Ammonia-Water Mixtures in Microscale Geometries for Miniaturized Absorption Systems Desorption of Ammonia-Water Mixtures in Microscale Geometries for Miniaturized," Ph.D. Dissertation, G. W. Woodruff School of Mechanical Engineering, Georgia Institute of Technology.

[87] Span, R., and Wagner, W., 1996, "A New Equation of State for Carbon Dioxide Covering the Fluid Region from the Triple-point Temperature to 1100 K at Pressures up to 800 MPa," J. Phys. Chem. Ref. Data, **25**(6), pp. 1509–1596.

Appendix A: Property Algorithms

As indicated in Section 2.1, sCO_2 material properties are evaluated at each simulation time step, and precise curve fits are needed to account for sharp variations in the pseudo-critical region. Curve fits were developed for specific heat (c_p), dynamic viscosity (μ), and Prandtl number (Pr) at reduced pressure of $P_r = 1.1$, to match the experimental conditions. Thermal conductivity $k = c_p\mu/\mathrm{Pr}$ was evaluated indirectly from the formulae for c_p, μ and Pr. These curve fits were developed as a function of relative temperature: $T_r = T - T_{pc}$, where T_{pc} is the pseudocritical temperature at a given pressure. Because there is sharp variation of material properties trends near the pseudo-critical temperature T_{pc}, two separate curve fit formulations (*i.e.*, $f_1(T_r)$ for $T_r < 0$ and $f_2(T_r)$ for $T_r \geq 0$, respectively) were used for μ and Pr. To ensure smoothness across T_{pc}, a blending function was defined for the reduced temperature range of $-1 \leq T_r \leq 1$ as follows:

$$\begin{cases} \gamma = (T_r + 1)/2 \\ f(T_r) = \gamma f_2(T_r) + (1-\gamma) f_1(T_r) \end{cases} \quad for \quad -1 \leq T_r \leq 1 \tag{A.1}$$

The proposed formulation for dynamic viscosity (μ) is:

$$\mu(T_r) = \begin{cases} a_0 + \sum_{i=1}^{2} a_i exp(b_i T_r) & for \quad T_r < 0 \\ c_0 + \sum_{i=1}^{2} c_i exp(d_i T_r) & for \quad T_r \geq 0 \end{cases} \tag{A.2}$$

in which a_0, a_i, b_i, c_0, c_i, and d_i are constant coefficients for the curve fit (Table A.1). The plot of reported μ [69] vs. the curve fit (eqn. A.2) is shown in Fig. A.1 (AAD < 1%).

Table A.1. Empirical constant coefficients for μ curve fit

P_r	a_0	a_1	b_1	a_2	b_2	c_0	c_1	d_1	c_2	d_2
1.1	3.467e-4	-2.983e-4	6.374e-3	-1.442e-5	4.87e-1	1.415e-5	7.802e-6	-1.304e-1	4.953e-6	4.149e-3

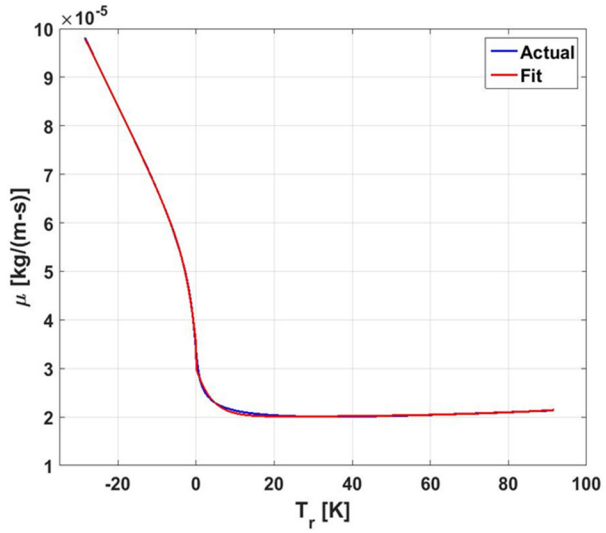

Figure A.1. Plot of reported μ [69]versus fitted curve for $P_r = 1.1$

The proposed fit for Prandtl number (Pr) is:

$$\mathrm{Pr}(T_r) = \begin{cases} a_0 + \sum_{i=1}^{2} a_i exp(b_i T_r) & for \quad T_r < 0 \\ c_0 + \sum_{i=1}^{2} c_i exp(d_i T_r) & for \quad T_r \geq 0 \end{cases} \tag{A.3}$$

in which $a_0, a_i, b_i, c_0, c_i,$ and d_i are constant coefficients for the curve fit (Table A.2). The plot of reported Pr values [70] vs. the curve fit (eqn. A.3) is shown in Fig. A.2 (AAD < 2%).

Table A.2. Empirical constant coefficients for Pr curve fits

P_r	a_0	a_1	b_1	a_2	b_2	c_0	c_1	d_1	c_2	d_2
1.1	2.083	2.834	0.1279	8.351	0.8194	0.797	8.407	-0.4741	1.225	-0.03032

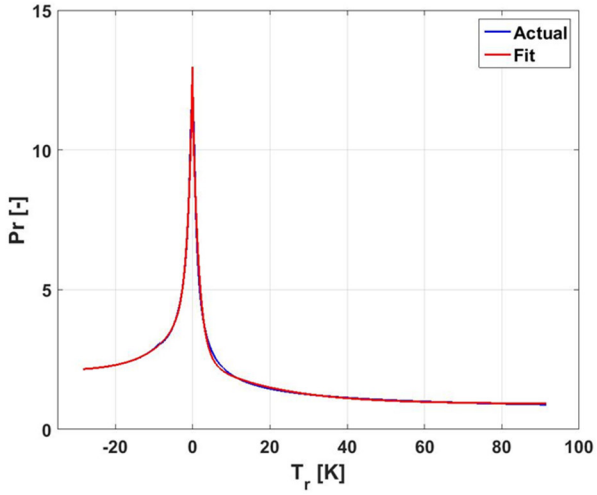

Figure A.2. Plot of reported Pr [70] versus fitted curve for $P_r = 1.1$

Initially, we attempted to use formulations for enthalpy and specific heat derived directly from equations of state. However, the resulting analytic (or implicit) formulations contained polynomial series that could diverge during solution (*e.g.*, if extreme values were evaluated at intermediate iterations). We therefore developed an explicit curve fit for c_p with improved numerical stability. c_p is fit with an exponential series. This leads to an "error function" series for enthalpy, which is well-bounded and monotonic with temperature.

The proposed curve fit for c_p is:

$$T_{clamp} = max\big(min\big(T, T_{pc} + T_{band}\big), T_{pc} - T_{band}\big)$$

$$c_p(T_r) = \begin{cases} c_{p,L} + \sum_{i=1}^{4} a_i exp\left(-\left(\frac{T_r}{b_i}\right)^2\right) & if\ T_{clamp} \le T_{pc} \\ c_{p,G} + \sum_{i=1}^{4} a_i exp\left(-\left(\frac{T_r}{b_i}\right)^2\right) & if\ T_{clamp} > T_{pc} \end{cases} \quad \text{(A.4)}$$

Here, a_i and b_i are constant coefficients for the curve fit (Table A.3). T_{pc} and T_{band} stand for the pseudo-critical temperature (i.e., $T_r = 0$, where the peak of c_p occurs), and the temperature difference from the peak to the point where c_p curve behaves asymptotically (see Fig. A.3), respectively. It should be noted that T_{clamp} was defined to confine the usage of these two curve fits to the temperature range where $T_{pc} - T_{band} < T < T_{pc} + T_{band}$. The specific heat is assumed constant for temperatures far from T_{pc} ($c_{p,L}$ for $T \ll T_{pc}$ and $c_{p,G}$ for $T \gg T_{pc}$.). Here, $T_{band} = 30\ K$ was used to cover all the range in which c_p varies with temperature. The plot of reported c_p [87] vs. the curve fit (Eqn. A.4) is shown in Fig. A.3 (AAD < 5%).

Table A.3. Empirical constant coefficients for c_p curve fits

P_r	a_1	b_1	a_2	b_2	a_3	b_3	a_4	b_4
1.1	10000	0.45	10000	1.5	5500	4.5	2000	14.5

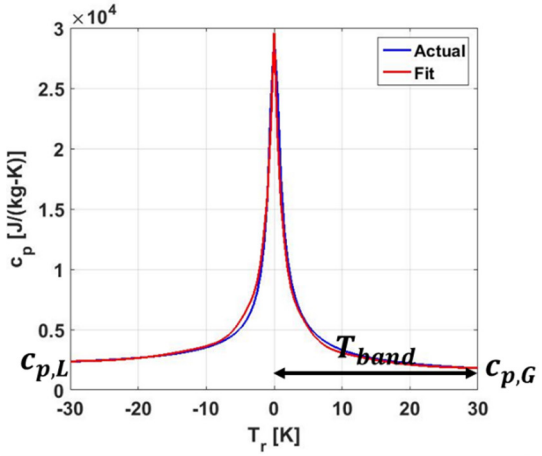

Figure A.3. Plot of reported c_p [87] versus fitted curve for $P_r = 1.1$

Fluid density (ρ) is evaluated using the Peng-Robinson equation of state [68] with AAD < 5% relative to [87].

Appendix B: Effects of Cyclic Domain Approximation on Simulation Results

Simulations in Sections 3-4 employ channel domains with heated walls and cyclic coupling between inlet and outlet planes. This approach effectively tracks a specific mass of fluid as it travels through a channel rather than a specific section of a channel, as measured in reference experiments [24]. This effects a transformation from space (flow evolving along channel length) to time (evolving flow of a fluid mass in time). This method significantly reduces computational costs (~25× here), but does not capture axial variation of fluid properties present in the experiments. Test simulations are performed here to estimate the impact of this approximation on heat transfer quantities of interest.

The test simulations are for 2-D flow between parallel plates and employ an unsteady RANS model (k-ω SST). This framework can capture global effects due to axial property variation with low computational cost relative to the LES studies in Sections 3-4. The 2D channel height is H = 737 μm with bulk reduced pressure P_r = 1.1, mass flux G = 500 kg m^{-2} s^{-1}, and top- and bottom-wall temperatures of T_w = 392.5 K (same as Case 7 in Table 4). The mesh resolution is the same as the "Finer" resolution mesh used in Case 7. At this pressure, the bulk fluid density reduces ~22% from T_{bulk} = 295 – 306 K. Based on heat transfer and friction-factor correlations at T_{bulk} = 300 K, the acceleration pressure drop gradient due to fluid expansion (3100 Pa m^{-1}) should exceed the frictional pressure gradient of 2870 Pa m^{-1}. If axial property variations significantly effect heat transfer predictions for sCO_2 channel flow at such conditions, they should manifest in this case that has strong property-variation induced hydrodynamic forces.

First, a cyclic inlet-outlet implementation is evaluated with a domain length of 5 mm (same as LES cases in Sections 2-3). sCO_2 is initialized in the domain with fully developed turbulent profiles of velocity and turbulence fields (k, ω) and uniform temperature 289.3 K. The fluid is cycled through the domain for 0.08 s and reaches a final bulk temperature of 307.6 K. Next, a corresponding full-channel-length flow-through (non-cyclic) implementation is evaluated with a 2.5 mm long adiabatic entrance

section and a 75 mm heated section with T_w = 392.5 K. The inlet conditions to the adiabatic section for u, k, ω, and T are the same as the initial conditions used in the cyclic implementation. The simulation is evaluated for 0.14 s to establish quasi-steady conditions along the full channel length ($\bar{u}$ ~ 0.8 m s^{-1}, $L/\bar{u}$ ~ 0.1 s). Data is then collected for each time step from t = 0.14 s to 0.15 s (~10 cycles based on $H/\bar{u}$ ~ 90 ms). The heated portion of the full-length domain is divided into 100 equal length "bins" (Δz = 750 μm). Time- and space-averaged flow temperature and wall heat flux are obtained for each bin. Corresponding average HTC values are obtained from the cyclic study for the periods in which the bulk fluid temperature is between the average inlet and outlet temperatures of each bin in the full-length study.

After a settling period (cyclic case T_{bulk}(t = 0.02 – 0.08 s) = 295 – 306 K), corresponding HTCs match between the cyclic and full-length simulations within ±8% (Fig. B.1). This deviation is due in part to the unsteady/random nature of both simulations. The overall average HTC deviation for T_{bulk} = 295 – 306 K is 3%. Qualitative similarity of overall flow behavior can be seen in Fig. B.2, which presents the density field from the two implementations for T_{bulk} ~ 300 K. This suggests that for the studied conditions, even when hydrodynamic effects due to axial property variation are significant ($|\nabla p_{acc}| > |\nabla p_f|$), the cyclic domain approximation introduces ≲5% error in heat transfer predictions.

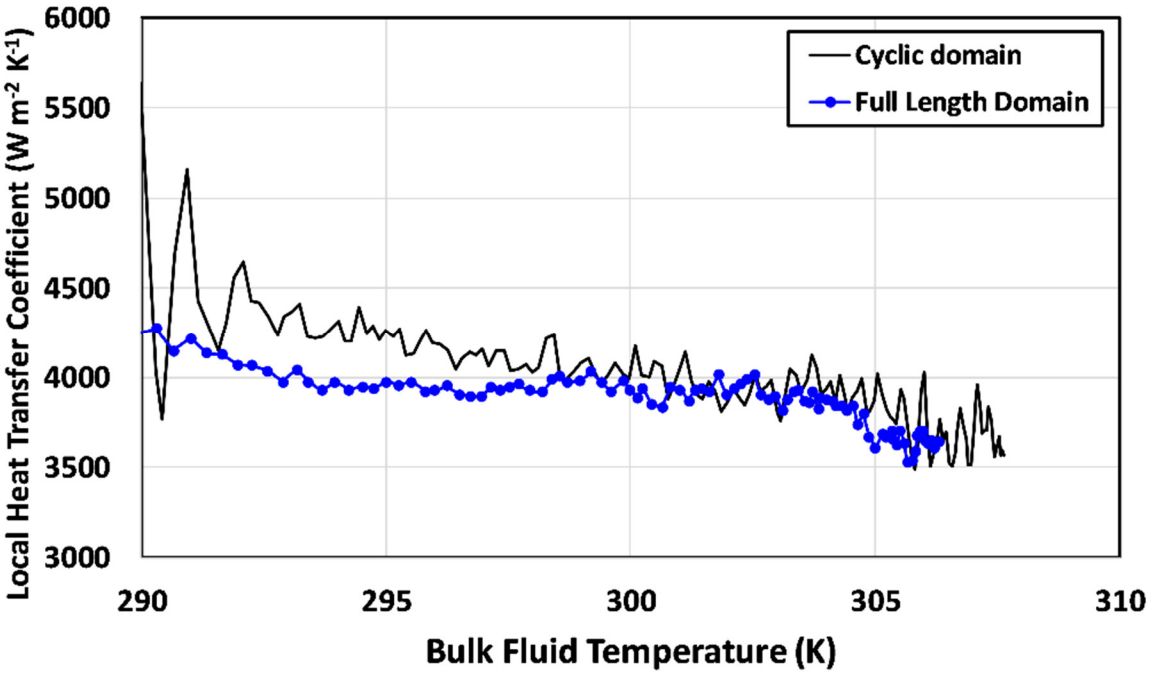

Figure B.1. Comparison of local heat transfer coefficient vs. bulk sCO2 flow temperature using cyclic and full-length domains

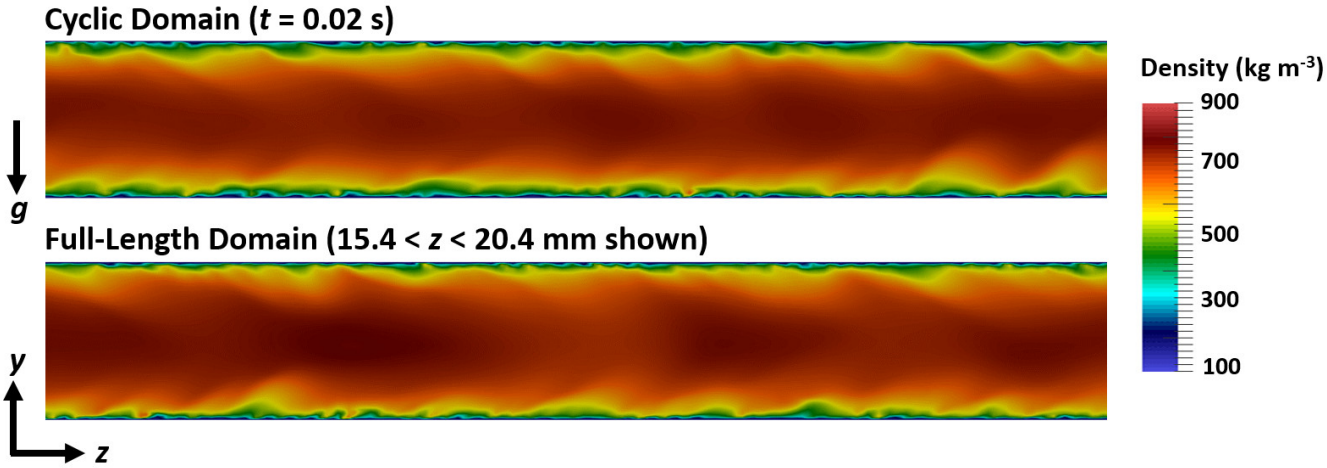

Figure B.2. Comparison of density fields from cyclic and full-length domains for T_{bulk} ~ 300 K, indicating qualitative similarity between simulation approaches.